Polymer 323 (2025) 128191

Contents lists available at ScienceDirect

Polymer

journal homepage: www.elsevier.com/locate/polymer

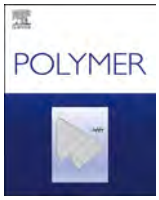

Highly practical multifunctional radiative cooling films for multi-temperature applications

Xiongbo Yang [a,b,1], Wendi Fan [a,b,1], Ruizhen Xu [a,b,*], Junmei Zhang [a,b], Qihao Dai [a], Long Wang [a,b], Xinyu Tan [a,**], Guiguang Qi [a], Yulong Qiao [a], Paul K. Chu [c]

[a] Hubei Provincial Engineering Research Center for Solar Energy High-value Utilization and Green Conversion, China Three Gorges University, Yichang, Hubei, 443002, PR China

[b] College of Science, China Three Gorges University, Yichang, Hubei, 443002, PR China

[c] Department of Physics, Department of Materials Science and Engineering, and Department of Biomedical Engineering, City University of Hong Kong, 999077, Hong Kong, China

ARTICLE INFO

Keywords:
Radiative cooling
Multifunctional
Multi-temperature application

ABSTRACT

Passive daytime radiative cooling is a green, sustainable technology, however there are challenges in incorporating multifunctional radiative cooling technologies. In this paper, a biomimetic structure (PTP, porous tetra-needle zinc oxide whisker polydimethylsiloxane) with a needle-like structure on the surface and a porous structure in the interior is prepared by a simple process using inexpensive tetra-needle zinc oxide whiskers (T-ZnOw) as the filler particles and polydimethylsiloxane (PDMS) as the binder, which possesses the desired radiative cooling properties, and at the same time, it combines the anti-aging, thermal control flame retarding, and superhydrophobic properties. PTP film exhibits ideal reflectance (0.91) and emissivity (0.99), with an average temperature difference of 15.5 °C compared to Al, and maintains good radiative cooling performance under UV irradiation for 1000 h. The thermal conductivity of the PTP film is 0.931 W m^{-1} k^{-1}. In the outdoor cooling test with a heat source, the average temperature difference is 13.3 °C compared to Al. The surface water contact angle (WCA) is 153.25° and the superhydrophobicity is maintained after more than 1400 h of aging. As a result, the PTP film has large potential in multi-temperature applications, such as buildings, factory sheds, and electrical appliances.

1. Introduction

In the pursuit of a cool environment in hot weather, food preservation, and outdoor work, air conditioning systems are used. However, air conditioners require a large electrical load, and power generation by conventional sources exacerbates global climate change and environmental pollution. For example, the temperature in Antarctica in 2020 exceeded 20 °C for the first time, and global warming may become the norm by 2050 [1–6]. In the context of carbon neutrality, people are exploring how to use as little or no fossil energy to achieve cooling effects, spurring the development of passive daytime radiative cooling (PDRC). PDRC is a sustainable and environmentally friendly passive cooling technology without using fossil energy [7,8]. Materials with good PDRC properties have two features: high reflection of sunlight in the wavelength range of 0.3–2.5 μm and high infrared thermal emissivity in the atmospheric window in the wavelength range of 8–13 μm, so that excess heat on the surface of the materials can be transported through the atmospheric window to the colder outside environment [9]. Radiative cooling is not only applied in practical production [10,11] and daily life [12–14], but also has led to the development of novel biomimetic materials that exhibit ideal cooling performance [15]. Radiative cooling has been applied to buildings and clothing, for example, porous radiative cooling films [16–18], polymers doped with inorganic salts and other particles [19–21], multi-layer laminated films [22], textiles with nanostructures or nanoparticles, and so on [23,24]. However, many of them do not meet the commercial requirements. Firstly,

* Corresponding author. Hubei Provincial Engineering Research Center for Solar Energy High-value Utilization and Green Conversion, China Three Gorges University, Yichang, Hubei, 443002, PR China.

** Corresponding author.

E-mail addresses: xurz@ctgu.edu.cn (R. Xu), tanxin@ctgu.edu.cn (X. Tan).

[1] These authors contributed equally to this work: Xiongbo Yang, Wendi Fan.

https://doi.org/10.1016/j.polymer.2025.128191
Received 28 October 2024; Received in revised form 17 January 2025; Accepted 23 February 2025
Available online 24 February 2025

the surface is easy to dust, so the radiative cooling capacity is reduced. Secondly, the micro-nanometer surface structure of the radiative cooling film is easily damaged by external abrasion, consequently losing superhydrophobicity. Thirdly, the polymer tends to be flammable, posing fire hazards. Therefore, new radiative cooling materials with self-cleaning, abrasion resistance, flame-retardancy, and aging resistance are highly desirable. In the food industry, the materials should have antimicrobial capability. In outdoor environments, the radiative cooling film must be able to withstand rain and sunlight while possessing adequate thermal conductivity in order that the heat can be reflected to the external environment.

At this stage, some radiative cooling technologies integrated with other functions have emerged, for example, porous Polymethyl Methacrylate (PMMA) [25,26], and a PDMS composite cooling film with superhydrophobic surfaces [27,28], which enable self-cleaning function; Cellulose acetate/zinc oxide nanocomposite film with antimicrobial properties for food preservation and transportation [29,30]; Preparation of high thermal conductivity boron nitride and high-density polyethylene composites by melt blending method [31]. Composites reflect sunlight, conduct heat, and are flame retardant. The combination of the above radiative cooling technology with other functions enables it to be used in more aspects, but there are some limitations, porous PDMS and PMMA have insufficient abrasion resistance [32]; Cellulose acetate/zinc oxide nanocomposite films without self-cleaning function; Boron nitride and polyethylene composites are costly and not suitable for large-scale applications. This shows that there are still challenges for a multifunctional, low-cost radiative cooling technology.

The Cyphochilus is reported to be a species of ladybug with an ultra-white shell, which is attributed to the many needle-like structures on the outside of the shell as well as a large number of porous structures on the inside, the combination of which facilitates its reflection and emission of sunlight [33]. Based on this kind of bionic structure, we used a physical mixture of tetra-needle zinc oxide whiskers (T-ZnOw), PDMS, and n-hexane and evaporated the film to form a bionic film possessing a needle-like structure on the surface and a porous structure inside. T-ZnOw provides the needle-like structure, PDMS is used as an adhesive, and hexane is used as a solvent, and the porous structure is formed by evaporation phase separation.

T-ZnOw is a white solid powder, with a special four-needle three-dimensional structure with the angle between any two needles being 109°28′. They have favorable properties such as the absorption of UV radiation [34,35], antimicrobial capability [34,36], thermal conductivity [37,38], flame retardancy [37], abrasion resistance [39], and superhydrophobicity [40], but they have not been applied in radiative cooling, which would have a high practicality if it could be combined with the above-described capabilities. In addition, T-ZnOw is being used for the first time in radiative cooling. Meanwhile, the PDMS atmospheric window band has strong thermal emissivity, mainly due to Si–CH_3 vibration (1265 cm^{-1}), Si–O–Si vibrations (1,085, 1,078, 1,060, and 1025 cm^{-1}), Si–OH vibrations (910, 865, and 844 cm^{-1}), and –CH_3 rocking vibration (802 cm^{-1}) [41], thus compensating for the lack of T-ZnOw emission in the atmospheric window. PDMS is often used in thermal conductive systems [42–44].

In this work, a white radiative cooling thin film (PTP) of porous doped particles is invented. The interactions of the three materials produce thin films with the bio-inspired structure. Due to the excellent properties of T-ZnOw particles, the PTP film has radiation cooling properties combined with aging resistance, flame retardancy, and superhydrophobicity, making it a practical and multifunctional radiative cooling film.

2. Materials and methods

2.1. Materials

PDMS elastomer material A and curing agent B were purchased from Shanghai Meter Trading Co., Ltd., China. N-hexane (AR≥97.0 %) was obtained from Tianjin Fuyu Fine Chemical Co., Ltd., China. The tetra-needle zinc oxide whiskers (T-ZnOw, angle 109° 28 ′, diameter 0.5–5 μm, length 10–50 μm) were bought from Hangzhou Jikang New Material Co., Ltd. And the commercial radiative cooling white paint (The entire text is expressed in white paint) was provided by Muyaju Sanitary Ware Co., Ltd.

2.2. Sample preparation

T-ZnOw is used as the filler particle, PDMS polymer as the adhesive, and n-hexane as the solvent for PDMS. Simple physical mixing is performed to prepare the suspension, and the porous materials are fabricated by thermal phase separation. Step (1): The PDMS elastomer material A was added to a flask with n-hexane with a ratio of 1:1 and stirred magnetically for 15 min to become homogeneous. Step (2): T-ZnOw (60 wt%) was added to the mixture in step (1) and stirred magnetically for 10 min. Step (3): Curing agent B with PDMS elastomer material A with a ratio of 1:10 was mixed and stirred magnetically for 10 min. Step (4): The homogeneous mixture in step (3) was placed on a clean substrate by a rubber-tipped dropper. The BEVS 1806B/150 adjustable squeegee was used to adjust the thickness. Uniform scraping was carried out to form a flat coating which was dried in an oven at 80 °C for 1.5 h.

2.3. Characterization

Scanning electron microscopy (SEM, JSM-7500F, JEOL) was used to examine the cross-sectional morphology of the films. The solar reflectance spectra were acquired on the NIR Fourier transform spectrometer (PE Frontier NIR, USA, wavelength range: 0.3–2.5 μm), and the atmospheric window emissivity spectra were collected on the Fourier transform infrared spectrometer (PE Fourier Transform, USA, wavelength range: 2.5–25 μm). The water contact angle (WCA) was measured by the static water droplet contact angle meter (Beijing Zhongchen Digital Technology Equipment Co., Ltd.), and the average was obtained from three randomly selected locations on the sample. FTIR was conducted on the spectrometer (PE, USA) (600 - 4000 cm^{-1}). X-ray diffraction (XRD) was carried out on the X-ray diffractometer (SmartLab 9 kW). The thermal conductivity was determined by a laser thermal conductivity meter (NETZSCH LFA467), and the thermogravimetric analysis was conducted from 0 to 1000 °C on the thermal analyzer (STA 449 F5). The resistance to UV aging was assessed using a UV accelerated test chamber (KINSGEO).

3. Results and discussion

3.1. Characterization of PTP film

As shown in Fig. 1a, PTP film is a bionic-like film possessing a large number of needle and porous structures on the surface and a large number of porous structures inside. The needles and pores form rough micro- and nanostructures, which are favorable for improving its reflectivity, emissivity and WCA. Fig. 1b–c confirm the porous structure with a large number of exposed needle-like structures of T-ZnOw. Porosity is about 11.4 μm (Fig. S1). The pores are also observed from the lateral SEM images resembling a ceramic structure (Fig. 1d and e). Porosity is about 17.4 μm (Fig. S2). The pores are produced by thermotropic phase separation during heating, and the tetra-needle-like three-dimensional structure of the T-ZnOw particles serves as a stabilizing support. Fig. 1f shows a 40 × 60 cm optical photograph of a PTP film with ultra-high whiteness due to the large number of particles and porous structure. The 40 × 60 cm PTP film demonstrates the capability of being prepared over a large area, while the ultra-high whiteness enhances its radiative cooling performance. Fig. S3 shows that the PTP film possesses good flexibility under different forms of deformation such as

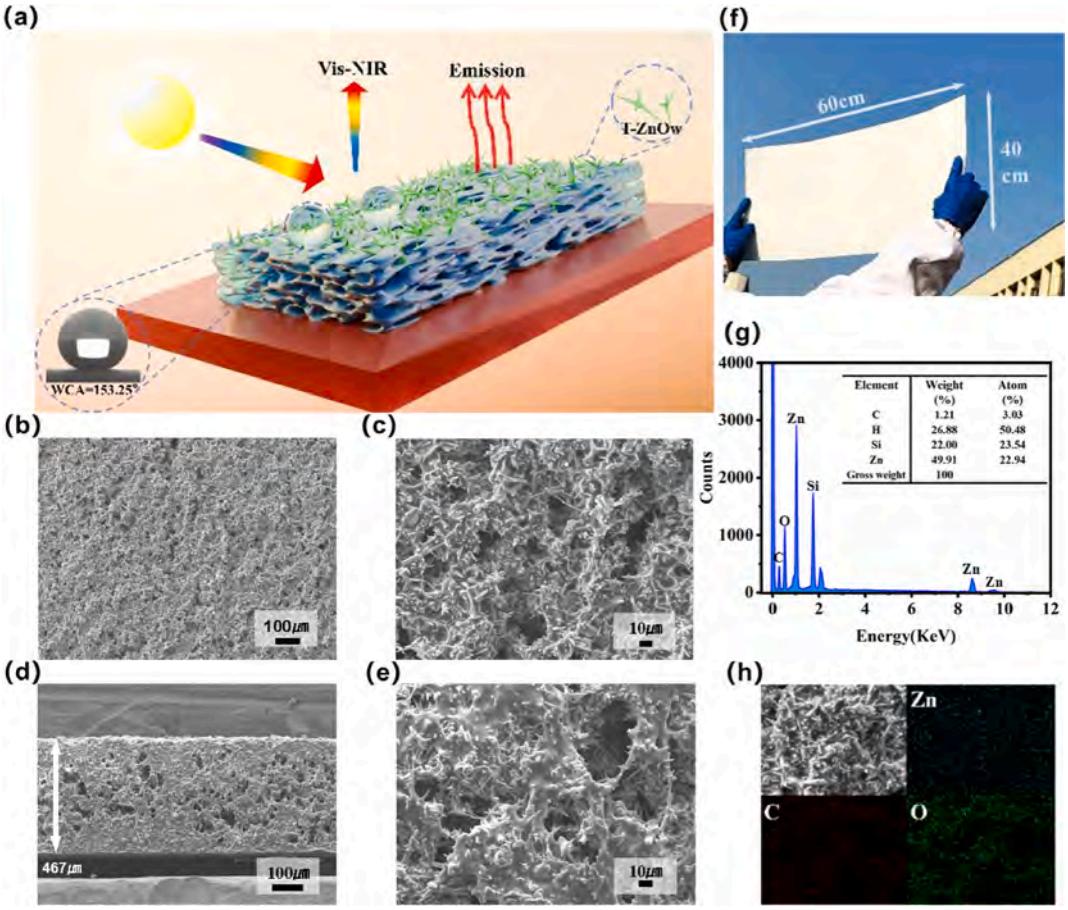

Fig. 1. Characterization of the PTP film. (a) Schematic of the PTP film. (b) Magnified 100x SEM image of the surface side of the PTP film. (c) SEM image with 500x magnification corresponding to (b). (d) Cross section magnified 100x SEM image of PTP film. (e) SEM image with 500x magnification corresponding to (d). (f) Optical photograph of a 40 × 60 cm PTP film. (g) EDS spectrum of PTP film. (h) Elemental maps of PTP film.

folding, twisting, and stretching. In addition, the mechanical properties of PTP films are tested for tensile strength, gravel impact resistance, and tensile cycling, which show that PTP films have good mechanical properties (Figs. S4–6). Fig. 1g indicates the presence of Zn, O, C, and Si and a Zn concentration of about 50 wt% in line with the mass fraction of the particles added to the PTP films. Fig. 1h shows that Zn, C, and O are uniformly distributed, indicating that T-ZnOw and PDMS are evenly dispersed without agglomeration. Fig. S7 XRD test results show the crystallization peaks associated with PTP films having with T-ZnOw particles having a counterpart.

3.2. Optical and anti-aging properties

The effectiveness of the radiative cooling effect is largely influenced by the optical properties of the films. The PTP radiative cooling films have excellent optical properties such as reflectance and emissivity as shown in Fig. 2a–c. The different mass fractions of particles and film thickness affect the optical properties. Under the conditions of the same thickness but different mass fractions, a particle mass fraction of 60 wt% is selected. On one hand, the reflectance and emissivity difference between 60 wt% and 70 wt% is not big, and the emissivity curve is also relatively flat when the particle mass fraction is 60 wt%. On the other hand, when the mass fraction is greater than 50 wt%, the surface of the film is better ornamental (Fig. S8). The film flexibility degrades if the particle mass fraction is too large. Under the conditions of the same mass fraction but different thicknesses, a thickness of 400 μm is chosen. The reflectance of the 400 μm film exceeds 0.9 in the 0.3–2.5 μm band, and the reflectance does not change appreciably with increasing thickness. Moreover, the cost is considered. In summary, we select a particle mass fraction of 60 wt% and a thickness of 400 μm. As for the same thickness (400 μm), the average reflectance in the sunlight spectrum (0.3–2.5 μm) of the PTP film with a particle mass fraction of 60 wt% is as high as 0.91 (Note S1. defines the calculation method), which is higher than those of white paint (0.71) by a factor of 1.35 and PDMS (0.0016) by a factor of 633. The strong absorption peaks in the 0.3–0.5 μm band are attributed to the ability of T-ZnOw to absorb UV light. The average emissivity in the atmospheric window (8–13 μm) is as high as 0.99, which is higher than those of white paint (0.96) and PDMS (0.94). A comprehensive comparison of the performance of PTP films with other similar radiative cooling films has also been made to show that they have superior properties (Table 1).

The high reflectance of PTP films can be attributed to the high refractive index filler and the porous structure. According to Mie scattering theory, scattering can occur at sizes comparable to the wavelength of the sun, and multiple sizes can broaden the scattering range [53]. T-ZnOw is a high refractive index filler (2.008–2.029) with a center diameter range of 0.5–5 μm (Fig. S9), so T-ZnOw is a multi-size-distributed particle while the size magnitude is comparable to the wavelength of the incident light, thereby broadening the Mie scattering range of photons. Meanwhile, the needle-like structures are widely distributed on the surface of the film and the pore walls (Fig. 1c) and have refractive index (n) differences with air and the polymer matrix. Due to the high specific surface area of the needle-like structures (needle length 10–50 μm, diameter 0–5 μm), multiple interfaces are formed at the film surface and pore walls, which ultimately lead to strong scattering of photons at the interfaces [29,31,54]. The reflectance

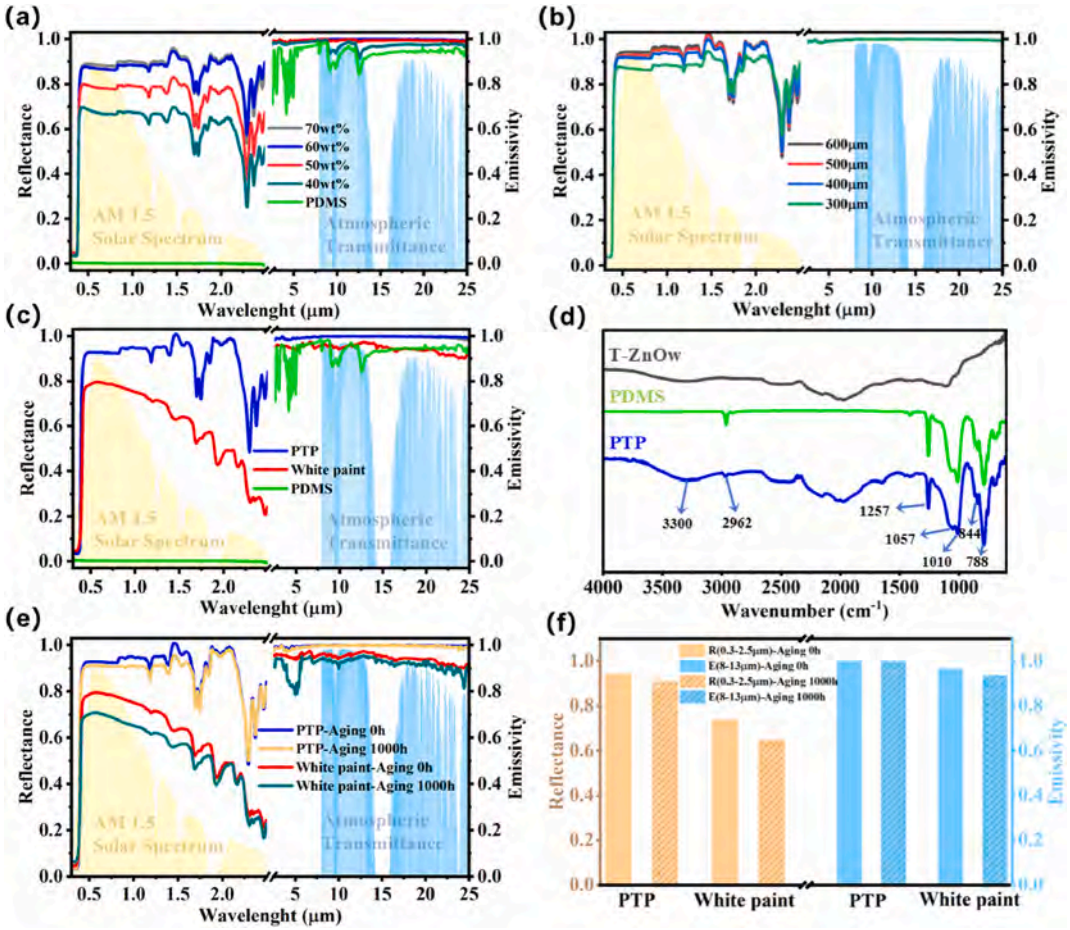

Fig. 2. Optical properties. (a) Comparison of reflectance and emissivity for particle mass fractions of 0, 40, 50, 60, and 70 wt% in PTP films. (b) Comparison of reflectance and emissivity of PTP films with thicknesses of 300, 400, 500, and 600 μm. (c) Comparison of reflectance and emissivity of PTP film with 60 wt% and 400 μm, white paint with 400 μm, and PDMS film with 400 μm. (d) FTIR spectra of PTP film, PDMS film, and T-ZnOw particles. (e) Reflectance and emissivity of PTP, white paint films before and after UV aging in the UV accelerated test chamber for 1000 h. (f) Average reflectance and emissivity of PTP and white paint films before and after UV aging for 1000 h in the 0.3–2.5 μm and 8–13 μm bands.

Table 1
Comparison of PTP film performance with other similar radiative cooling films.

Samples	Reflectance (0.3–2.5 μm)	Emissivity (8–13 μm)	References
PTP	0.91	0.99	This Work
Porous PDMS	0.73	0.99	[8]
Superhydrophobic PDMS film	0.85	0.95	[9]
Hollow SiO_2/PDMS	0.9	0.92	[45]
BN/DCPDA	0.78	0.96	[21]
Bionically Mxene-SEBS/TiO_2 film	0.66	0.89	[46]
Flame retardant MA/PA film	0.89	0.91	[47]

of film with T-ZnOw particles increases by 10.8 % than that of film with uniform size zinc oxide. (Fig. S10). In addition, porous structures with a pore size distribution comparable to the wavelength of the incident light and a refractive index mismatch with air can also cause Mie scattering of photons and thus increase reflectance [55].

According to Kirchhoff's law, radiant coolers can enhance thermal radiation by introducing a series of infrared absorption bands [56]. The IR absorption bands of PTP, PDMS, and T-ZnOw are shown in the FTIR spectrogram (Fig. 2d), confirming their ability to enhance thermal radiation. The absorption peaks at 788, 844, 1,010, 1,257, and 2962 cm^{-1} are from the Si–O, Si–C, Si–O–Si, Si–CH_3, and –CH_3 stretching vibrations [24,36], and these molecules all exhibit vibrations that effectively coincide with the atmospheric window, suggesting that the PTP thin films have strong absorption in the atmospheric window (770 - 1250 cm^{-1}). The absorption peak at 1060 cm^{-1} corresponds to an asymmetric deformation of –CH_3 consistent with PDMS, while the absorption peak of T-ZnOw at 3300 cm^{-1} is a stretching vibration of –OH [57]. In summary, it can be seen that PTP is rich in infrared absorption bonds and possesses high emissivity capability. At the same time, different regions within the needle exhibit varying degrees of lattice distortion, leading to higher values of the imaginary part of the refractive index (k) over a broad range of optical wavelengths [58,59]. As a result, the needle-like structure can absorb infrared light more strongly compared to other parts. In addition, the atomic crystal surface (1010) (Fig. S7) can vibrate to convert light energy into kinetic and thermal energy [60]. The emissivity of T-ZnOw particles increases by 10.8 % than that of uniform size zinc oxide (Fig. S11). In porous structures, it is possible to increase IR absorption/emission through multiple diffuse reflections, thus enhancing radiative heat exchange [26,61,62].

Radiative cooling films need to have some resistance to UV aging for outdoor cooling applications. In order to improve the reflectance and emissivity of the PTP film while not compromising the UV aging resistance, UV aging tests (Fig. S12) are performed according to ASTM D 7897–18 with simulated sunlight. The UV irradiation intensity is set to 0.89 W/m^2, the temperature is 60 °C. After the UV aging test for 1000 h, which is equal to one year of solar irradiation exposure in Florida [63], the reflectance (0.3–2.5 μm) of the PTP film decreases from 0.910 to

0.901, showing a reduction of ~0.9 %, but it still remains above 0.9 in this band while maintaining the good reflectance. The emissivity (8–13 μm) decreases slightly from~0.9992 to 0.9986. In comparison, the reflectance (0.3–2.5 μm) of white paint decreases from 0.71 to 0.63, representing a reduction of 8 %. The emissivity (8–13 μm) diminishes from 0.966 to 0.936, showing a reduction of 3 % (Fig. 2e–f). Therefore, the aging resistance of the PTP film, both in terms of reflectance and emissivity, is higher than that of white paint. According to the optical picture (Fig. S13), the PTP film still exhibits a very high whiteness after aging. On the contrary, a slight yellow color change and flaking is observed after the white paint aging test. In general, the reflectance and emissivity of PTP films have good UV aging resistance boding well for outdoor applications in bright sunlight.

3.3. Radiative cooling properties and applications

In order to understand the radiation refrigeration performance of PTP film, an outdoor test is performed (Fig. 3a) using a cooling test box, thermocouples, a handheld weather station, and a solar irradiator. The dimensions of the test foam box are 15 × 15 × 15 cm^3, with aluminum foil wrapped around the outer edge to prevent the polyethylene foam from absorbing the surrounding heat. A 5 × 5 × 5 cm^3 internal chamber at the top of the box to place the test samples, thermocouples, and so on. A handheld weather station is used to record the ambient temperature, wind speed and humidity at the location of the test box. A solar radiometer is used to measure the intensity of sunlight, and an infrared thermal imager is used to capture the thermal images.

On June 12, 2024, the cooling test was conducted on the roof of the Materials and Chemistry building in Yichang City (longitude 111.32, latitude 30.72). The purpose of the sealing PE film is to prevent the influence of the heat flux in the vicinity, wind, and humidity on the experimental results. According to Fig. 3b, the solar irradiance is 0.58 kW m^{-2}, and the maximum temperature difference is 17.7 °C compared to the Al substrate temperature, which is higher than those of white paint of 9.4 °C and PDMS of 5.8 °C. The average temperature difference is 8.0 °C and higher than that of white paint of 5.3 °C and PDMS of 3.5 °C (Fig. S14). At the time of the highest temperature (11 a.m.–2 p.m.) with a solar irradiance of ~0.87 kW m^{-2}, the average temperature difference of the PTP film compared to the Al substrate temperature is 15.5 °C, which is higher than those of white paint of 7.5 °C and PDMS of 5.0 °C. At night (8 p.m.–11:59 p.m.) with a solar irradiance of 0 kW m^{-2}, the average temperature difference is 4.8 °C, which is higher than those of white paint of 4.7 °C and PDMS of 4.6 °C. The detailed comparison is presented in Table S1.

Cooling tests are also performed without sealing the PE film and in sunny weather. In the unsealed PE film cooling test (Figs. S15–16), the solar irradiance on that day (9 a.m.–11:59 p.m.) is 0.59 kW m^{-2}. The maximum temperature difference is 11.5 °C with an average of 6.1 °C compared to the Al substrate, and the maximum temperature difference is 10.5 °C with an average of 5.6 °C compared to the ambient temperature. At the time with the highest temperature (11 a.m.–2 p.m.), the solar irradiance is 0.87 kW m^{-2}, and the average temperature difference is 8.9 °C compared to the Al substrate and 7.6 °C compared to the ambient temperature. At night (8 p.m.–11:59 p.m.) with a solar

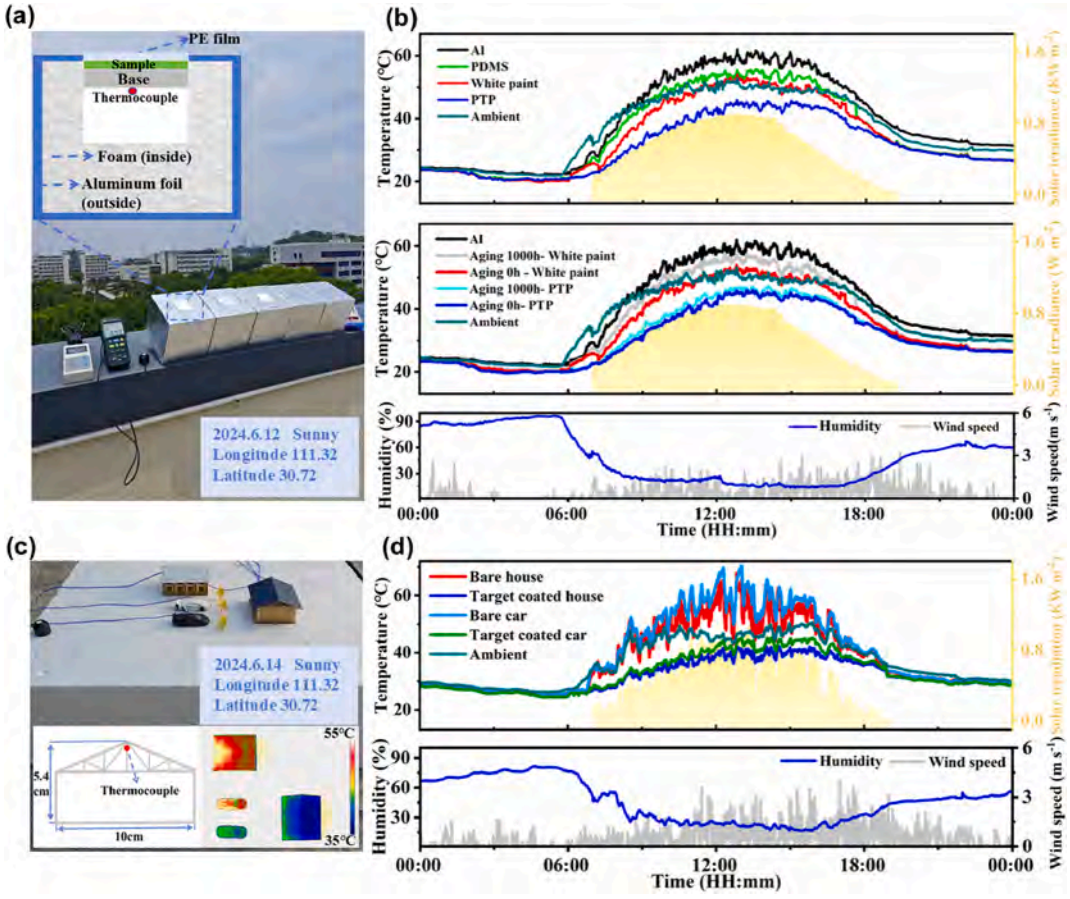

Fig. 3. Radiative Cooling Properties and Applications. (a) Test site, schematic diagram of the test box, weather data on June 12, 2024, and local latitude and longitude. (b) Temperature curves of the sealed PE film cooling test, temperature curves before and after 1000 h of aging resistance, and solar irradiance, wind speed, and humidity on the same day. (c) Simulated application test site, simulated application with a house, a car, weather data of 2024.6.14, schematic of a house, and infrared thermography of a house and a car with and without a PTP film cover using an infrared thermal imager. (d) Temperature curves for target-coated rooms, bare houses, target-coated cars, and bare cars versus solar irradiance, wind speed, and humidity on the same day.

irradiance of 0 kW m^{-2}, the average temperature difference is 1.9 °C compared to the Al substrate temperature and 1.8 °C compared to the ambient temperature. The detailed comparison is presented in Table S2.

On June 10, 2024, the temperature difference of the sealed PE film is assessed in cloudy weather (Figs. S17–18). The solar irradiance is 0.74 kW m^{-2} during the time with the highest temperature (11 a.m.–2 p.m.), the maximum temperature difference is 16.3 °C, and the average temperature difference is 11.0 °C compared to the Al substrate temperature. Table S3 shows the detailed comparison. In summary, the PTP radiative cooling film delivers strong radiative cooling performance during the day and night, but cloudy weather can have a temperature reduction effect.

In order to visually verify the aging resistance of PTP radiative cooling films, samples before and after aging are tested for outdoor cooling performance at the locations shown in Fig. 3a. The solar irradiance is 0.58 kW m^{-2} (Fig. 3b). The cooling effect of the PTP film before the anti-aging test is similar to that after, showing an average temperature difference between the two of 0.6 °C. The maximum temperature difference between the anti-aging PTP film and the Al substrate afterward is 17.4 °C, and the average temperature difference is 7.9 °C (Fig. S19). The average temperature difference between the white paint before and after the anti-aging test is 1.8 °C. The maximum temperature difference between the white paint after anti-aging and the Al substrate is 6.4 °C, and the average temperature difference is 2.8 °C. Table S4 shows the detailed comparison. In conclusion, the cooling effect of the PTP film after the anti-aging test for 1000 h is better than that of white paint.

A house and a car model (Fig. 3c) are chosen to simulate the real application of cooling tests. The dimensions of the house are 10 × 10 × 5.4 cm, and those of the car are 8 cm long and 4 cm wide. The temperature testing point on a house is located on the roof, and that of the car is located inside the car. On June 14, 2024, the solar irradiance is 0.5 kW m^{-2} (Fig. 3d and S20). The coated house shows a maximum temperature difference of 25.8 °C and an average temperature difference of 6.2 °C compared to the bare house. The maximum temperature difference of the coated car is 25.1 °C and the average temperature difference is 6.9 °C compared to the bare car temperature. Table S5 presents the detailed comparison. According to the infrared thermography in Fig. 3c, the house or car covered with PTP film shows a significant temperature reduction effect. The cooling test is also conducted in cloudy weather (Figs. S21–22) and the results are shown in Table S6. All in all, the PTP film has large potential in outdoor construction, automotive, and other applications.

3.4. Thermal conductivity and thermal stability

For electrical appliances working outdoors, such as air conditioners, high-voltage electrical appliances, and so on, exposure to sunlight may cause deleterious effects. On one hand, sunlight brings heat, and on the other hand, the appliances themselves generate heat. If the temperature inside the appliance cannot be lowered, the efficiency will be reduced, which will lead to aging over a long period of time, and a serious fire may result. Therefore, it is important to have not only excellent radiative cooling properties, but also good thermal conductivity and thermal stability.

The thermal conductivity of the PDMS film is 0.19 W m^{-1} k^{-1} (Fig. 4a). In order to improve the thermal conductivity, it is useful to fill the polymer matrix with thermally conductive materials [64,65]. When the concentration of T-ZnOw particles is 40 wt%, its thermal conductivity is 0.415 W m^{-1} k^{-1}. The thermal conductivity can be improved by increasing the amount of conductive materials, whereas the small amount will lead to “sea-island” effect [66,67]. For a particle mass fraction of 60 wt%, the thermal conductivity is 0.931 W m^{-1} k^{-1}, which is 490 % compared to the PDMS film. Although the porous structure has internal heat conduction path defects to a certain extent, as shown in Fig. S23, which makes it susceptible to phonon-interfacial scattering during the heat transfer process and inevitably forms a “thermal resistance” [68], T-ZnOw has a good heat conduction ability and is expected to be used in thermal management and heat dissipation of electronic devices [37]. At the same time, benefiting from the tetra-needle structure and the aspect ratio of T-ZnOw, it can be combined with the polymer to form a three-dimensional thermal conductivity network,

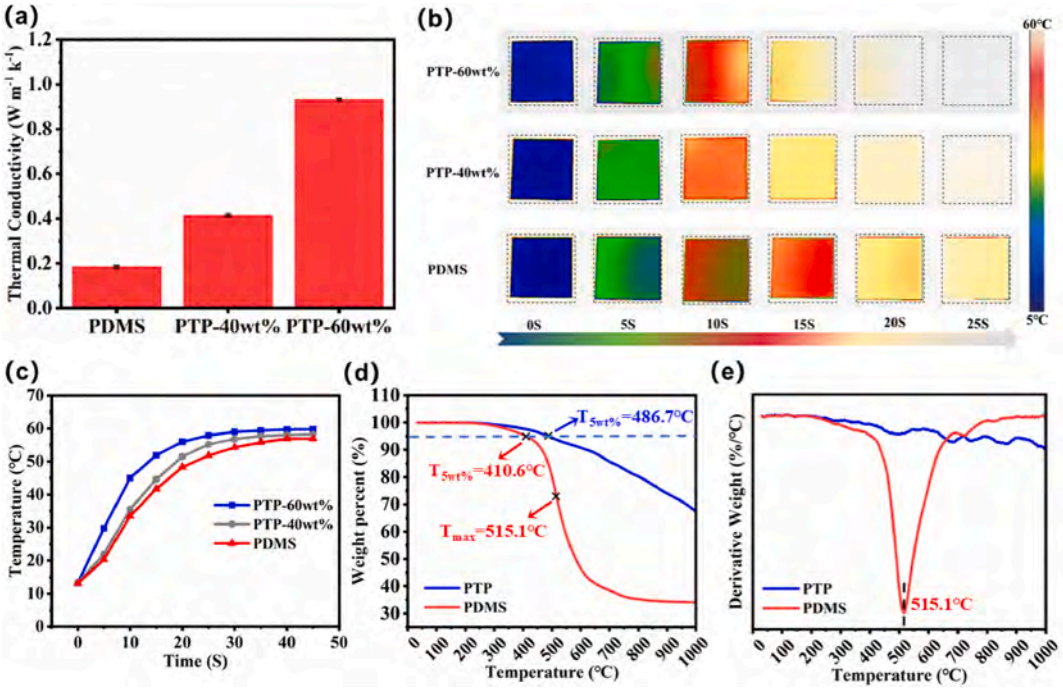

Fig. 4. Thermal conductivity and thermal stability test of PTP films. (a) Thermal conductivity of PDMS, 40 wt% PTP, and 60 wt% PTP films. (b) Infrared thermography changes of PDMS, 40 wt% PTP, and 60 wt% PTP films on a predetermined 60 °C heating table. (c) Temperature variations of PDMS, 40 wt% PTP and 60 wt% PTP films corresponding to Figure (b). (d–e) Thermogravimetric analysis tests of PTP, PDMS films.

which leads to efficient heat flow paths inside the film [57].

To visually verify the thermal conductivity, three samples, PTP-60 wt %, PTP-40 wt%, and PDMS, are placed on a heating table preheated to 60 °C (Fig. S24). An infrared thermography camera is utilized to record in real time the process from the beginning until the temperature stabilizes. According to IR thermography (Fig. 4b), and the temperature curve (Fig. 4c), the initial IR thermography color of the three samples is basically the same (at 13.1 °C). With increasing time (5 s as a unit), the IR thermography color change (temperature change) of PTP-60 wt% is significantly faster than that of the other two samples, PTP-40 wt% and lastly PDMS. At 25 s, PTP-60 wt% has essentially the same color as the infrared thermography of the heated table (59.8 °C), while PTP-40 wt% is close to the heated table (58.2 °C) and PDMS is 55.8 °C. The stabilization temperature of PTP-60 wt% (59.8 °C) is 1.6 °C higher than that of PTP-40 wt% (58.2 °C) and 4 °C higher than PDMS (55.8 °C). Hence, the incorporation of T-ZnOw improves the thermal conductivity of the film.

We evaluate the thermal stability of PTP and PDMS films by thermogravimetric tests. In a nitrogen atmosphere, according to the TG curves (Fig. 4d), the thermal decomposition temperature ($T_{5wt\%}$) for 5 % mass loss of PTP films is 486.7 °C, which is higher than that of PDMS films (410.6 °C). According to the DTG (Fig. 4e) curves, the PDMS film starts to decompose at 515.1 °C (T_{max}). At 1000 °C, the char residue of PDMS is 34.1 %. The PTP films do not exhibit a maximum decomposition temperature within the tested range of 0–1000 °C, unlike the PDMS films. The char residue for the PTP films at 1000 °C is 67.5 %. It is evident that the pyrolysis ability of high content of T-ZnOw particles enhances the char residue of PTP films. As shown in Table 2, the various thermogravimetric key parameters of the PTP films are significantly superior compared to other flame retarding materials containing ZnO. Therefore, the PTP films have strong thermal stability.

3.5. Radiant cooling properties with a heat source and flame retardancy

In order to verify that PTP films can be applied to cool electrical appliances with heat sources outdoors, an experimental device box that simulates the environment of electrical appliances is designed. As shown in Fig. 5a, a 5 × 5 × 5 cm^3 internal cavity is dug inside a 15 × 15 × 15 cm^3 square foam box, and a heating table is placed on the bottom of the cavity at 60 °C to simulate the usual working temperature of electrical appliances. A test sample is placed on top of the cavity, and a thermocouple is attached to the bottom of the sample to measure the temperature. On June 11, 2024, the outdoor cooling test with a heat source was conducted on the roof of the Materials and Chemistry building in Yichang City (longitude 111.32, latitude 30.72) (Fig. 5a). According to Fig. 5b–c, the solar irradiation (11:30 a.m. to 2 p.m.) is 0.74 kW m^{-2}. The maximum temperature difference of 17.2 °C and the average temperature difference of 13.3 °C for the PTP film compared to the Al substrate are higher than the maximum temperature difference of 13.4 °C and the average temperature difference of 10.3 °C for the white paint, and higher than the maximum temperature difference of 8.6 °C and the average temperature difference of 6.2 °C for the PDMS. Table S7 shows the detailed comparison. The wind speed and humidity are shown in Fig. S25. After the testing device is moved indoors (Figs. S26–27), the maximum temperature difference of the PTP film is 13.5 °C, and the average temperature difference is 9.1 °C compared with the Al substrate, which is higher than the maximum temperature difference of 9.2 °C and the average temperature difference of 6.1 °C for white paint and higher than the maximum temperature difference of 6.6 °C and the average temperature difference of 4.5 °C for PDMS. Table S8 shows the detailed comparison. In summary, the PTP film has good outdoor radiative cooling properties such as the ability to reflect sunlight, rapid transmission of internal heat, and transferring heat to the outside ambient.

Table 2
Key parameters of the thermogravimetric test of PTP films in the nitrogen atmosphere and comparison with the literature.

Samples	$T_{5wt\%}$ (°C)	T_{max} (°C)	Residue (%)	References
PTP	486.7	681.4	67.5	This Work
IFR/mZnO	420	498	9.7	[48]
PTR-40	324.1	452.7	5.2	[49]
PP/24%Si-IFR/2%SiZnO	315	388	15.6	[50]
PAXY13–100	225	254	40.5	[51]
EP/5MCA/3MTZ	369	395	6.45	[52]

In order to cope with the fire safety hazards posed by electrical appliances, we have conducted flame retardant test on PTP film. It is understood that zinc oxide is a flame retardant [48,69]. According to the thermogravimetric test results, PTP is analyzed to have good thermal stability, indicating good conditions for flame retardancy. In the flame retardant test (Fig. 5d), a commercial blue flame blowtorch is used for the PDMS and PTP films. In the first cycle, the PDMS film heated for 1 s shows spontaneous combustion and generates smoke, and heating stops immediately. Spontaneous combustion occurs for 7 s before extinguishing. The PDMS film changes from transparent to gray and shows obvious deformation. In the second cycle, heating for 3 s starts spontaneous combustion and smoke generation. Heating stops, but the PDMS film burns violently emitting thick smoke and cannot be extinguished until it burns out after 18 s. As for the PTP film in the first heating cycle, heating for 5 s leads to spontaneous combustion and smoke generation. After heating ceases, it extinguishes after 1 s. In the second cycle, heating for 5 s starts spontaneous combustion and smoke generation. After heating stops, it extinguishes after 1 s. In the third cycle, spontaneous combustion and smoke generation do not occur until 7 s. After heating stops and after 1 s, the color of the film becomes light gray, and the film remains relatively intact. In summary, the PDMS film burns out when heated for two cycles, while the PTP film spontaneously combusts in the first two cycles of heating, but can be instantly extinguished by stopping heating. It does not spontaneously combust in the third cycle of heating, and changes to a light gray color after heating stops. Throughout the cyclic heating process, the PTP film takes longer to combust spontaneously than the PDMS film, and the number of heating cycles is more than that of the PDMS film. The PDMS film burns to carbon after two cycles of heating, while the PTP film remains relatively intact after three cycles of heating.

There are several possible reasons for the flame-retardant properties of PTP films. Firstly, T-ZnOw is not significantly decomposed at high temperatures (0–1000 °C) according to the TG test (Fig. 4d–e). Secondly, T-ZnOw promotes the production of CO_2 and H_2O from PDMS, reduces the O_2 concentration and temperature around the PDMS film, and slows combustion [52]. As shown in Fig. S28, the Si–C and Si–CH_3 peaks at 844 and 1257 cm^{-1} disappear after burning. Finally, T-ZnOw can absorb a large amount of heat quickly through the three-dimensional thermal conduction pathway, thus acting as a physical barrier to lower the ambient temperature of the PDMS film. Therefore, the PTP films have good flame retarding properties to improve the fire safety (Fig. S29).

3.6. Self-cleaning and durability

The special micro- and nano-needle and porous structure render the PTP film surface superhydrophobic. As shown in Fig. 6a, the WCA of T-ZnOw with different mass percentages changes. With increasing mass percentage, the WCA increases. The WCA of pure PDMS is 105.5° ± 1.7° and the WSA is 180° ± 0°. When the content of T-ZnOw is 30 wt%, the WCA goes up by 11° due to the relatively smooth surface of T-ZnOw encapsulated by PDMS without the porous structure. When the content is 50 wt%, a part of the needle-like structure of T-ZnOw is exposed to increase the surface roughness, and the WCA changes to 144.67° ± 1.3°and the WSA changes to 35.5° ± 1.8°. When the content of T-ZnOw is 60 wt%, the WCA is 153.25° ± 0.7° and the WSA is 9.2° ± 0.3° representing superhydrophobicity. The low surface chemical energies of polymers and micro- and nanoparticles combined with the low coverage of polymers provide self-cleaning surfaces. Although the polymers and micro- and nanoparticles can interact, a certain distribution and surface

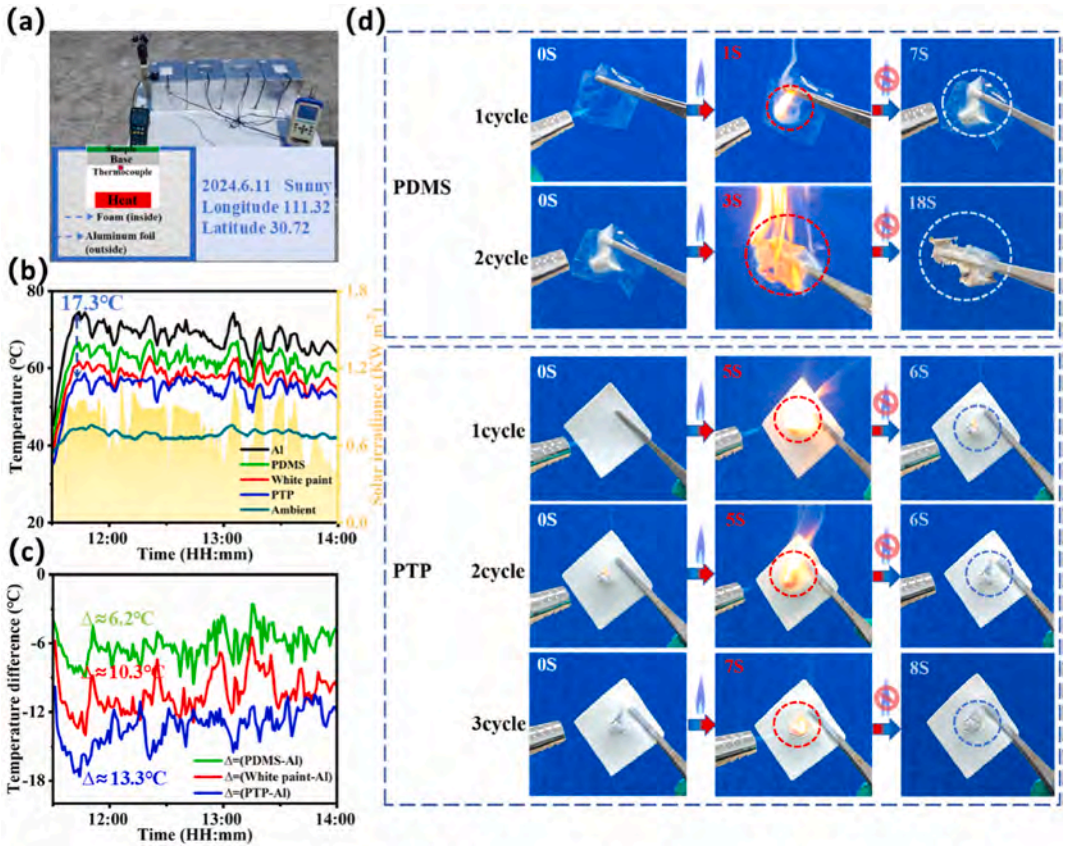

Fig. 5. Radiative cooling properties with a heat source and flame retardancy. (a) Outdoor test site with a heat source, schematic of test box with a heat source, weather data on June 11, 2024, and local latitude and longitude. (b) Outdoor temperature curves with a heat source and solar irradiance. (c) Temperature differences corresponding to (b). (d) Flame retarding test of PDMS and PTP films for a commercial blue flame gun. (For interpretation of the references to color in this figure legend, the reader is referred to the Web version of this article.)

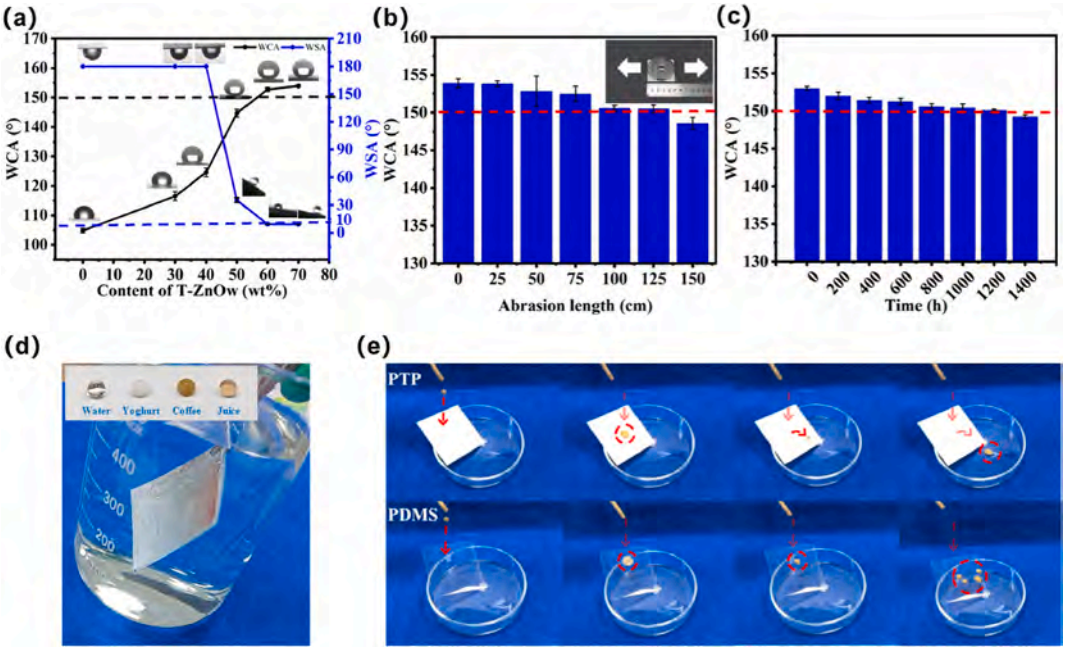

Fig. 6. Self-cleaning and durability of PTP films. (a)WCA and WSA values of PTP films with different particle mass fractions. (b) WCA values of PTP film after abrasion on 600 mesh sandpaper. (c) WCA values of PTP film after UV accelerated aging chamber test. (d) Silver mirror phenomenon and the state of various liquids on the surface of the film. (e) Self-cleaning test in PTP, PDMS film by simulating muddy water dripping into the film.

roughness are required to produce superhydrophobicity and self-cleaning properties [70]. On the other hand, there is a transition from the Wenzel state to the Cassie-Baxter state, where the roughness of the coating surface goes from low to high (Fig. S30). The contact area of the droplets with the surface decreases, and more air is trapped on the surface of the film [36].

The self-cleaning durability of the PTP film is evaluated to ensure its suitability for long-term outdoor use. A friction test using 600 mesh sandpaper and a 200 g load is performed. The hydrophobic angle is measured every 25 cm, and at the end of each cycle, the WCA decreases. At 125 cm, the hydrophobic angle maintains over 150° as shown in Fig. 6b. The UV intensity is set to 0.89 W/m^2, the temperature is 60 °C. The WCA is measured every 200 h (Fig. 6c). After 1200 h (the equivalent of over 500 days of outdoor exposure in Florida), the WCA remains stable above 150°. This indicates excellent UV resistance for the T-ZnOw needle-like structure, allowing prolonged sunlight exposure without significant structural damage. The PTP film thus exhibits good hydrophobic durability, which is promising for long-term outdoor applications. Fig. 6d shows that a reflective silver layer forms on the surface of the film because the film is isolated by air, thus preventing water from wetting it. 60 μl droplets of water, yogurt, coffee, and juice can form on the film. As shown in Fig. 6e, the PDMS film is tested for self-cleaning with the PTP film. A dropper is used to suck up the muddy water and drop it onto the two films. About 0.05 ml of muddy water (simulating the volume of a raindrop) is dropped each time, and the PTP film bounces the muddy water, which eventually falls to the Petri dish, thus avoiding the contact between the muddy water and film surface, confirming the self-cleaning effect. In contrast, the PDMS film is unable to bounce the muddy water off the surface of the film; instead, it is stuck to the surface of the film. The experimental results in Fig. 6d and e show that the PTP film has a strong self-cleaning ability to effectively prevent contaminants from affecting the radiative cooling performance of the film.

4. Conclusion

The PTP film, a radiative cooling film with porous doped particles, has many desirable properties. It shows needle-like bionic as well as porous ceramic-like structures with whiteness and flexibility. In the sunlight spectral band (0.3–2.5 μm), the reflectance is 0.91, and the atmospheric window (8–13 μm) emissivity is 0.99, besides excellent anti-ultraviolet aging. Simulated outdoor exposure for a year reveals that the reflectance is still as high as 0.9, and the emissivity is basically unchanged. In the outdoor cooling test without a heat source, the average temperature difference compared to the Al from 11:00 a.m. to 2 p.m. is 15.5 °C. The PTP film has a thermal conductivity of 0.931 W m^{-1} k^{-1} and shows average temperature differences as high as 13.3 °C in the outdoor cooling tests with a heat source and 9.1 °C indoors. The high thermal decomposition capacity makes it flame retarding, thus mitigating fire risks. The needle-like and porous micro-nano structures yield superhydrophobicity and reduce the impact of dust and muddy water on the degradation of the radiative cooling properties. In addition, the strong hydrophobic durability enables outdoor applications for extended periods of time. As a result of the multiple functionalities, the materials have large commercial potential.

CRediT authorship contribution statement

Xiongbo Yang: Writing – review & editing, Funding acquisition. **Wendi Fan:** Writing – review & editing, Writing – original draft, Software, Methodology, Investigation, Formal analysis, Data curation. **Ruizhen Xu:** Writing – review & editing, Funding acquisition. **Junmei Zhang:** Methodology. **Qihao Dai:** Investigation. **Long Wang:** Methodology. **Xinyu Tan:** Methodology, Funding acquisition. **Guiguang Qi:** Supervision. **Yulong Qiao:** Methodology. **Paul K. Chu:** Writing – review & editing, Funding acquisition.

Declaration of competing interest

The authors declare that there are no known competing financial interests or personal relationships that might influence the work reported here.

Acknowledgments

This work was supported by the National Nature Science Foundation of China (No.520071404),111 Project (D20015) of China, Yichang City Natural Science Research Project (A24-3-001), and City University of Hong Kong Donation Research Grants (DON-RMG 9229021 and 9220061).

Appendix A. Supplementary data

Supplementary data to this article can be found online at https://doi.org/10.1016/j.polymer.2025.128191.

Data availability

Data will be made available on request.

References

[1] H.-D. Wang, C.-H. Xue, C.-Q. Ma, X.-X. Jin, M.-C. Huang, Y.-G. Wu, S.-Q. Lv, A.-J. Chang, J. Li, X.-J. Guo, Durable and scalable superhydrophobic colored composite coating for subambient daytime radiative cooling, ACS Sustainable Chem. Eng. 12 (2024) 1681–1693, https://doi.org/10.1021/acssuschemeng.3c07329.
[2] B. Gu, Z. Dai, H. Pan, D. Zhao, Integration of prolonged phase-change thermal storage material and radiative cooling textile for personal thermal management, Chem. Eng. J. 493 (2024) 152637, https://doi.org/10.1016/j.cej.2024.152637.
[3] M.-C. Huang, M. Yang, X.-J. Guo, C.-H. Xue, H.-D. Wang, C.-Q. Ma, Z. Bai, X. Zhou, Z. Wang, B.-Y. Liu, Y.-G. Wu, C.-W. Qiu, C. Hou, G. Tao, Scalable multifunctional radiative cooling materials, Prog. Mater. Sci. 137 (2023) 101144, https://doi.org/10.1016/j.pmatsci.2023.101144.
[4] Y. Dong, X. Zhang, L. Chen, W. Meng, C. Wang, Z. Cheng, H. Liang, F. Wang, Progress in passive daytime radiative cooling: a review from optical mechanism, performance test, and application, Renew. Sustain. Energy Rev. 188 (2023) 113801, https://doi.org/10.1016/j.rser.2023.113801.
[5] J. Liang, J. Wu, J. Guo, H. Li, X. Zhou, S. Liang, C.-W. Qiu, G. Tao, Radiative cooling for passive thermal management towards sustainable carbon neutrality, Natl. Sci. Rev. 10 (2023) nwac208, https://doi.org/10.1093/nsr/nwac208.
[6] S. Zhao, B. Da, F. Peng, B. Hu, C. Gao, K. Dai, G. Zheng, C. Liu, C. Shen, Facilely fabricated polyethylene film composed of directional microfibrils for passive radiative cooling, Polymer 299 (2024) 126979, https://doi.org/10.1016/j.polymer.2024.126979.
[7] X. Yang, J. Geng, R. Xu, X. Tan, M. Liu, S. Nie, S. Yao, S. Li, J. Zhang, Y. Tu, G. Qi, Y. Qiao, Self-cleaning energy-free PDMS@KL film for daytime radiative cooling, Mater. Lett. 350 (2023) 134831, https://doi.org/10.1016/j.matlet.2023.134831.
[8] J. Zhang, X. Yang, R. Xu, S. Li, G. Qi, X. Tan, An environmentally friendly porous PDMS film via a template method based for passive daytime radiative cooling, Mater. Lett. 357 (2024) 135686, https://doi.org/10.1016/j.matlet.2023.135686.
[9] S. Nie, X. Tan, X. Li, K. Wei, T. Xiao, L. Jiang, J. Geng, Y. Liu, W. Hu, X. Chen, Facile and environmentally-friendly fabrication of robust composite film with superhydrophobicity and radiative cooling property, Compos. Sci. Technol. 230 (2022) 109750, https://doi.org/10.1016/j.compscitech.2022.109750.
[10] W. Xie, C. Xiao, Y. Sun, Y. Fan, B. Zhao, D. Zhang, T. Fan, H. Zhou, Flexible photonic radiative cooling films: fundamentals, fabrication and applications, Adv. Funct. Mater. 33 (2023) 2305734, https://doi.org/10.1002/adfm.202305734.
[11] K. Bu, X. Huang, X. Li, H. Bao, Consistent assessment of the cooling performance of radiative cooling materials, Adv. Funct. Mater. 33 (2023) 2307191, https://doi.org/10.1002/adfm.202307191.
[12] S. Kim, S. Lee, J. Lee, H.W. Choi, W. Choi, Y.T. Kang, Passive isothermal film with self-switchable radiative cooling-driven water sorption layer for arid climate applications, Nat. Commun. 15 (2024) 8000, https://doi.org/10.1038/s41467-024-52328-z.
[13] P. Wang, H. Wang, Y. Sun, M. Zhang, S. Chen, C. Xiao, H. Zhou, Transparent grating-based metamaterials for dynamic infrared radiative regulation smart windows, Phys. Chem. Chem. Phys. 26 (2024) 16253–16260, https://doi.org/10.1039/D4CP01245C.
[14] J. Li, Y. Jiang, J. Liu, L. Wu, N. Xu, Z. Zhang, D. Zhao, G. Li, P. Wang, W. Li, B. Zhu, Y. Zhang, J. Zhu, A photosynthetically active radiative cooling film, Nat. Sustain. 7 (2024) 786–795, https://doi.org/10.1038/s41893-024-01350-6.
[15] X. Liu, C. Xiao, P. Wang, M. Yan, H. Wang, P. Xie, G. Liu, H. Zhou, D. Zhang, T. Fan, Biomimetic photonic multiform composite for high-performance radiative cooling, Adv. Opt. Mater. 9 (2021) 2101151, https://doi.org/10.1002/adom.202101151.

[16] J. Zhou, C. Ding, X. Zhang, D. Li, D. Yang, B. You, L. Wu, High-Durable, radiative-cooling, and heat-insulating flexible films enabled by a bioinspired dictyophora-like structure, ACS Appl. Mater. Interfaces (2023) 3c14310, https://doi.org/10.1021/acsami.3c14310 acsami.
[17] C. Xu, H. Lu, Z. Liu, N. Luo, A. Wei, Flexible piezoresistive sensors based on porous PDMS/CB composite materials prepared by the solvothermal method, J. Mater. Sci. Mater. Electron. 34 (2023) 906, https://doi.org/10.1007/s10854-023-10322-z.
[18] Q. Li, T. Duan, J. Shao, H. Yu, Fabrication method for structured porous polydimethylsiloxane (PDMS), J. Mater. Sci. 53 (2018) 11873–11882, https://doi.org/10.1007/s10853-018-2396-z.
[19] P. Das, S. Rudra, K.C. Maurya, B. Saha, Ultra-emissive MgO-PVDF polymer nanocomposite paint for passive daytime radiative cooling, Adv Mater. Tech. 8 (2023) 2301174, https://doi.org/10.1002/admt.202301174.
[20] Y. Xi, Y. Qi, Z. Mao, Z. Yang, J. Zhang, Surface hydrophobic modification of TiO2 and its application to preparing PMMA/TiO2 composite cool material with improved hydrophobicity and anti-icing property, Constr. Build. Mater. 266 (2021) 120916, https://doi.org/10.1016/j.conbuildmat.2020.120916.
[21] Q. Dai, X. Tan, G. Qi, X. Yang, B. Li, Z. Guo, J. Zhang, W. Hu, S. Li, C. Nguyen, X. Chen, Y. Xiao, P. Xiang, Durable and robust broadband radiative cooling coatings for multi-temperature scenarios, Sol. Energy 276 (2024) 112685, https://doi.org/10.1016/j.solener.2024.112685.
[22] Z. Hu, Y. Qiu, J. Zhou, Q. Li, Smart flexible porous bilayer for all-day dynamic passive cooling, Small Sci. (2024) 2300237, https://doi.org/10.1002/smsc.202300237.
[23] T. Wang, X. Wu, Q. Zhu, Y. Chen, S. Zhang, M. Gu, Y. Zhang, A scalable and durable polydimethylsiloxane-coated nanoporous polyethylene textile for daytime radiative cooling, Nanophotonics 0 (2023), https://doi.org/10.1515/nanoph-2023-0596.
[24] B. Gu, Q. Xu, H. Wang, H. Pan, D. Zhao, A hierarchically nanofibrous self-cleaning textile for efficient personal thermal management in severe hot and cold environments, ACS Nano 17 (2023) 18308–18317, https://doi.org/10.1021/acsnano.3c05460.
[25] X. Yu, M. Xue, Z. Yin, Y. Luo, Z. Hong, C. Xie, Y. Yang, Z. Ren, Flexible boron nitride composite membranes with high thermal conductivity, low dielectric constant and facile mass production, Compos. Sci. Technol. 222 (2022) 109400, https://doi.org/10.1016/j.compscitech.2022.109400.
[26] G. Qi, X. Tan, Y. Tu, X. Yang, Y. Qiao, Y. Wang, J. Geng, S. Yao, X. Chen, Ordered-porous-Array Polymethyl methacrylate films for radiative cooling, ACS Appl. Mater. Interfaces 14 (2022) 31277–31284, https://doi.org/10.1021/acsami.2c06809.
[27] Q. Zhai, Q. Zhu, Radiative cooling film with self-cleaning function, Sol. Energy Mater. Sol. Cell. 228 (2021) 111117, https://doi.org/10.1016/j.solmat.2021.111117.
[28] M.-C. Huang, C.-H. Xue, J. Huang, B.-Y. Liu, X.-J. Guo, Z.-X. Bai, R.-X. Wei, H.-D. Wang, M.-M. Du, S.-T. Jia, Z. Chen, Y. Lai, A hierarchically structured self-cleaning energy-free polymer film for daytime radiative cooling, Chem. Eng. J. 442 (2022) 136239, https://doi.org/10.1016/j.cej.2022.136239.
[29] K. Zhang, C. Mo, X. Tang, X. Lei, Hierarchically porous cellulose-based radiative cooler for zero-energy food preservation, ACS Sustainable Chem. Eng. 11 (2023) 7745–7754, https://doi.org/10.1021/acssuschemeng.3c00170.
[30] W.B. Han, H. Kang, S.-Y. Heo, Y. Ryu, G. Kim, G.-J. Ko, J.-W. Shin, T.-M. Jang, S. Han, J.H. Lim, C.-H. Eom, Y.M. Song, S.-W. Hwang, Stretchable and biodegradable composite films for disposable, antibacterial, radiative cooling system, Chem. Eng. J. 483 (2024) 149388, https://doi.org/10.1016/j.cej.2024.149388.
[31] W. Zhang, Y. Wang, H. Sun, C. Liu, C. Shen, X. Liu, Thermal conductive high-density polyethylene/boron nitride composites with high solar reflectivity for radiative cooling, Adv. Compos. Hybrid Mater. 6 (2023) 163, https://doi.org/10.1007/s42114-023-00739-9.
[32] W. Su, P. Cai, J. Darkwa, M. Hu, G. Kokogiannakis, C. Xu, L. Wang, Review of daytime radiative cooling technologies and control methods, Appl. Therm. Eng. 235 (2023) 121305, https://doi.org/10.1016/j.applthermaleng.2023.121305.
[33] L. Qi, W. Cai, T. Cui, B. Lin, Z. Feng, J. Gao, G. Jiang, W. Guo, C. Wang, B. Fei, J. Zhu, Y. Hu, W. Xing, L. Song, Bioinspired fireproof textiles with hierarchical micropore for radiative cooling and perspiration, Chem. Eng. J. 497 (2024) 154834, https://doi.org/10.1016/j.cej.2024.154834.
[34] H. Qiu, A. Gapeeva, S. Kaps, R. Adelung, M.J. Baum, Modification of nylon nets with poly(dimethylsiloxane)/tetrapodal-shaped ZnO composite for aquaculture biofouling control, ACS Appl. Polym. Mater. 3 (2021) 6598–6607, https://doi.org/10.1021/acsapm.1c01290.
[35] M. Li, S. Deng, Y. Yu, J. Jin, Y. Yang, X. Guo, Mechanical properties and microstructure of oil well cement stone enhanced with Tetra-needle like ZnO whiskers, Constr. Build. Mater. 135 (2017) 59–67, https://doi.org/10.1016/j.conbuildmat.2016.12.051.
[36] X. Zhou, Y. Luo, X. Tong, L. Zhu, Y. Wu, J. Lin, S. Huang, J. Ma, Superhydrophobic PDMS/SiNPs/T-ZnOw coating with reduced adhesion of Streptococcus mutans for dental caries prevention, Ceram. Int. 49 (2023) 6228–6237, https://doi.org/10.1016/j.ceramint.2022.10.271.
[37] H. Du, Y. Qi, W. Yu, J. Yin, H. Xie, T-shape ZnO whisker: a more effective thermal conductive filler than spherical particles for the thermal grease, Int. J. Heat Mass Tran. 112 (2017) 1052–1056, https://doi.org/10.1016/j.ijheatmasstransfer.2017.05.016.
[38] S. Nie, X. Zhang, J. Luo, Y. Liu, W. Yan, Synergistic effect of boron nitride and tetrapod-shaped zinc oxide whisker hybrid fillers on filler networks in thermal conductive HDPE composites, Polym. Compos. 38 (2017) 1902–1909, https://doi.org/10.1002/pc.23760.
[39] Z. Zhou, S. Liu, L. Gu, Studies on the strength and wear resistance of tetrapod-shaped ZnO whisker–reinforced rubber composites, J. Appl. Polym. Sci. 80 (2001) 1520–1525, https://doi.org/10.1002/app.1243.
[40] Y. Yamauchi, M. Tenjimbayashi, S. Samitsu, M. Naito, Durable and flexible superhydrophobic materials: abrasion/scratching/slicing/droplet impacting/bending/twisting-tolerant composite with porcupinefish-like structure, ACS Appl. Mater. Interfaces 11 (2019) 32381–32389, https://doi.org/10.1021/acsami.9b09524.
[41] S. Li, G. Du, M. Pan, X. Wang, X. Dong, T. Huang, D. Hu, T. Ren, X. Li, H. Chen, X. Mai, Scalable and sustainable hierarchical-morphology coatings for passive daytime radiative cooling, Adv. Compos. Hybrid Mater. 7 (2024) 15, https://doi.org/10.1007/s42114-023-00819-w.
[42] C. Li, X. Wang, Y. Li, H. Wang, Q. Tang, A. Hu, X. Chen, 3D modified graphene-carbon fiber hybridized skeleton/PDMS composites with high thermal conductivity, Compos. Sci. Technol. 225 (2022) 109499, https://doi.org/10.1016/j.compscitech.2022.109499.
[43] Y. Yang, R. Bi, W. Ren, Y. Sun, H. Zhao, H. Duan, Oriented rGO framework induced hBN confined network in PDMS for absorption enhanced EMI shielding and through-plane thermal conductivity, Compos. Sci. Technol. 243 (2023) 110259, https://doi.org/10.1016/j.compscitech.2023.110259.
[44] H. Liu, X. Su, R. Fu, B. Wu, X. Chen, The flexible film of SCF/BN/PDMS composites with high thermal conductivity and electrical insulation, Compos. Commun. 23 (2021) 100573, https://doi.org/10.1016/j.coco.2020.100573.
[45] J. Lee, D. Im, S. Sung, J. Yu, H. Kim, J. Lee, Y. Yoo, Scalable and efficient radiative cooling coatings using uniform-hollow silica spheres, Appl. Therm. Eng. 254 (2024) 123810, https://doi.org/10.1016/j.applthermaleng.2024.123810.
[46] Y. Zhao, F. Fang, Cephalopod-inspired Mxene-SEBS/TiO2 composite film for synergistic solar and infrared radiative heat management, Surf. Interfaces 51 (2024) 104565, https://doi.org/10.1016/j.surfin.2024.104565.
[47] W. Cai, B. Lin, L. Qi, T. Cui, Z. Li, J. Wang, S. Li, C. Cao, M. Ziaur Rahman, X. Hu, R. Yu, S. Shi, W. Xing, Y. Hu, J. Zhu, B. Fei, Bio-based and fireproof radiative cooling aerogel film: achieving higher sustainability and safety, Chem. Eng. J. 488 (2024) 150784, https://doi.org/10.1016/j.cej.2024.150784.
[48] Z. Liu, S. Xing, Y. Li, J. Sun, H. Li, X. Gu, S. Zhang, Surface modification of zinc oxide and its application in polypropylene with excellent fire performance and ultra-violet resistance, J. Colloid Interface Sci. (2024), https://doi.org/10.1016/j.jcis.2024.01.134. S0021979724001425.
[49] B. Liang, K. Liu, J. Dai, W. Chen, W. Lu, Polymer-type flame retardants based on a DOPO derivative for improving the flame retardancy of polyamide 6: Preparation, properties and flame retardancy mode of action, Polym. Degrad. Stabil. 225 (2024) 110807, https://doi.org/10.1016/j.polymdegradstab.2024.110807.
[50] M. Deng, Z. Zhang, J. Sun, X. Liu, H. Li, X. Gu, S. Zhang, Improving the flame retardancy and water resistance of polypropylene by introducing microcapsule flame retardant system and modified zinc oxide, Polym. Degrad. Stabil. 221 (2024) 110668, https://doi.org/10.1016/j.polymdegradstab.2024.110668.
[51] W.-M. Song, L.-Y. Zhang, P. Li, Y.-P. Ni, Y. Liu, The fabrication of flame-retardant viscose fabrics with phytic acid-based flame retardants: balancing efficient flame retardancy and tensile strength, Int. J. Biol. Macromol. 260 (2024) 129596, https://doi.org/10.1016/j.ijbiomac.2024.129596.
[52] G. Wang, Y. Shao, K. Niu, Q. He, Synthesis of a novel biobased tetrapod zinc oxide and synergy with melamine cyanurate to improve the flame retardancy and mechanical properties of epoxy resins, Colloids Surf. A Physicochem. Eng. Asp. 677 (2023) 132342, https://doi.org/10.1016/j.colsurfa.2023.132342.
[53] J. Xu, X. Wu, Y. Li, S. Zhao, F. Lan, A. Xi, Y. Huang, Y. Ding, R. Zhang, High-performance radiative cooling sunscreen, Nano Lett. (2024), https://doi.org/10.1021/acs.nanolett.4c04969 acs.nanolett.4c04969.
[54] X. Zhao, T. Li, H. Xie, H. Liu, L. Wang, Y. Qu, S.C. Li, S. Liu, A.H. Brozena, Z. Yu, J. Srebric, L. Hu, A solution-processed radiative cooling glass, Science 382 (2023) 684–691, https://doi.org/10.1126/science.adi2224.
[55] G. Qi, X. Tan, X. Yang, Y. Qiao, X. Li, Y. Wang, S. Chen, Y. Tu, S. Nie, K. Yan, Z. Kang, Anti-aging and flexible-porous-array films for radiative cooling, Sol. Energy Mater. Sol. Cell. 268 (2024) 112733, https://doi.org/10.1016/j.solmat.2024.112733.
[56] J. Huang, M. Li, D. Fan, Core-shell particles for devising high-performance full-day radiative cooling paint, Appl. Mater. Today 25 (2021) 101209, https://doi.org/10.1016/j.apmt.2021.101209.
[57] H. Chi, D. Liu, C. Ma, M. Song, P. Zhang, P. Dai, Simultaneously enhanced in-plane and out-of-plane thermal conductivity of a PI composite film by tetraneedle-like ZnO whiskers and BN nanosheets, ACS Appl. Polym. Mater. 5 (2023) 6909–6919, https://doi.org/10.1021/acsapm.3c00958.
[58] R. Wu, C. Xie, Formation of tetrapod ZnO nanowhiskers and its optical properties, Mater. Res. Bull. 39 (2004) 637–645, https://doi.org/10.1016/j.materresbull.2003.12.009.
[59] Y.K. Mishra, R. Adelung, ZnO tetrapod materials for functional applications, Mater. Today 21 (2018) 631–651, https://doi.org/10.1016/j.mattod.2017.11.003.
[60] K. Hagiwara, T. Yamazaki, S. Ozawa, Infrared spectroscopic study on adsorption of acetonitrile from solution onto several oxide surfaces at high pressure, J. Colloid Interface Sci. 170 (1995) 421–425, https://doi.org/10.1006/jcis.1995.1120.
[61] W. Hu, F. Zhang, X. Tan, Y. Tu, S. Nie, Antibacterial PVDF coral-like hierarchical structure composite film fabrication for self-cleaning and radiative cooling effect, ACS Appl. Mater. Interfaces 16 (2024) 19828–19837, https://doi.org/10.1021/acsami.4c01926.
[62] Y. Yan, P. Cui, S. Wu, H. Wei, S. Zhong, W. Sun, Dynamic fabrication of porous polymeric coating for efficient passive daytime radiative cooling using in-situ pore-formation strategy, Polymer 307 (2024) 127327, https://doi.org/10.1016/j.polymer.2024.127327.

[63] J. Song, W. Zhang, Z. Sun, M. Pan, F. Tian, X. Li, M. Ye, X. Deng, Durable radiative cooling against environmental aging, Nat. Commun. 13 (2022) 4805, https://doi.org/10.1038/s41467-022-32409-7.
[64] X. Yang, J. Zhu, D. Yang, J. Zhang, Y. Guo, X. Zhong, J. Kong, J. Gu, High-efficiency improvement of thermal conductivities for epoxy composites from synthesized liquid crystal epoxy followed by doping BN fillers, Compos. B Eng. 185 (2020) 107784, https://doi.org/10.1016/j.compositesb.2020.107784.
[65] F. Xu, P. Ye, J. Peng, H. Geng, Y. Cui, D. Bao, R. Lu, H. Zhu, Y. Zhu, H. Wang, Cerium methacrylate assisted preparation of highly thermally conductive and anticorrosive multifunctional coatings for heat conduction metals protection, Nano-Micro Lett. 15 (2023) 201, https://doi.org/10.1007/s40820-023-01163-w.
[66] R. Ji, S. Wang, X. Zhao, J. Zhang, Y. Zou, G. Chen, Y. Wang, Y. Huang, J. Ouyang, D. Jia, Y. Zhou, TiO2-BN/CNTs coating with radiative cooling and reduced friction, Chem. Eng. J. 493 (2024) 152802, https://doi.org/10.1016/j.cej.2024.152802.
[67] Y. Guo, K. Ruan, X. Shi, X. Yang, J. Gu, Factors affecting thermal conductivities of the polymers and polymer composites: a review, Compos. Sci. Technol. 193 (2020) 108134, https://doi.org/10.1016/j.compscitech.2020.108134.
[68] N. Burger, A. Laachachi, M. Ferriol, M. Lutz, V. Toniazzo, D. Ruch, Review of thermal conductivity in composites: mechanisms, parameters and theory, Prog. Polym. Sci. 61 (2016) 1–28, https://doi.org/10.1016/j.progpolymsci.2016.05.001.
[69] O. Nechyporchuk, H. Ulmefors, A. Teleman, Silica-rich regenerated cellulose fibers enabled by delayed dissolution of silica nanoparticles in strong alkali using zinc oxide, Carbohydr. Polym. 264 (2021) 118032, https://doi.org/10.1016/j.carbpol.2021.118032.
[70] A.I. Mendoza, R. Moriana, H. Hillborg, E. Strömberg, Super-hydrophobic zinc oxide/silicone rubber nanocomposite surfaces, Surf. Interfaces 14 (2019) 146–157, https://doi.org/10.1016/j.surfin.2018.12.008.

Supporting Information

Highly practical multifunctional radiative cooling films for multi-temperature applications

Xiongbo Yang[a,b,1], Wendi Fan[a,b,1], Ruizhen Xu[a,b,*], Junmei Zhang[a,b], Qihao Dai[a], Long Wang[a,b], Xinyu Tan[a,**], Guiguang Qi[a], Yulong Qiao[a], Paul K Chu[c]

[a] Hubei Provincial Engineering Research Center for Solar Energy High-value Utilization and Green Conversion, China Three Gorges University, Yichang, Hubei 443002, P. R. China

[b] College of Science, China Three Gorges University, Yichang, Hubei 443002, P. R. China

[c] Department of Physics, Department of Materials Science and Engineering, and Department of Biomedical Engineering, City University of Hong Kong, Hong Kong 999077, China

[1] These authors contributed equally to this work: Xiongbo Yang, Wendi Fan

[*]E-mail: xurz@ctgu.edu.cn; tanxin@ctgu.edu.cn

Note S1. Definitions of average solar reflectance, and thermal emittance.

The average solar reflectance ($\overline{R}_{\text{Solar}}$) is defined as shown in equation (1):

$$\overline{R}_{\text{Solar}} = \frac{\int_{0.3\mu m}^{2.5\mu m} I_{\text{Solar}}(\lambda) R(\lambda) d\lambda}{\int_{0.3\mu m}^{2.5\mu m} I_{\text{Solar}}(\lambda) d\lambda}, \quad (1)$$

where λ is the solar wavelength, $I_{\text{Solar}}(\lambda)$ is the normalized ASTM G173 global solar spectrum, and $R(\lambda)$ is the sample's spectral reflectance. Similarly, the thermal emittance $\overline{\varepsilon}_{(\lambda_1\text{-}\lambda_2)}$is defined as shown in equation (2):

$$\overline{\varepsilon}_{(\lambda_1\text{-}\lambda_2)} = \frac{\int_{\lambda_1}^{\lambda_2} I_{\text{bb}}(T,\lambda)\overline{\varepsilon}(T,\lambda) d\lambda}{\int_{\lambda_1}^{\lambda_2} I_{\text{bb}}(T,\lambda) d\lambda}, \quad (2)$$

where $\overline{\varepsilon}(T, \lambda)$ is the sample's spectral emittance and $I_{\text{bb}}(T,\lambda) = \frac{2c^2h}{\lambda^5} \frac{1}{e^{\frac{hc}{\lambda k_B T}} - 1}$ is indicating the solar intensity of the blackbody at the temperature T.

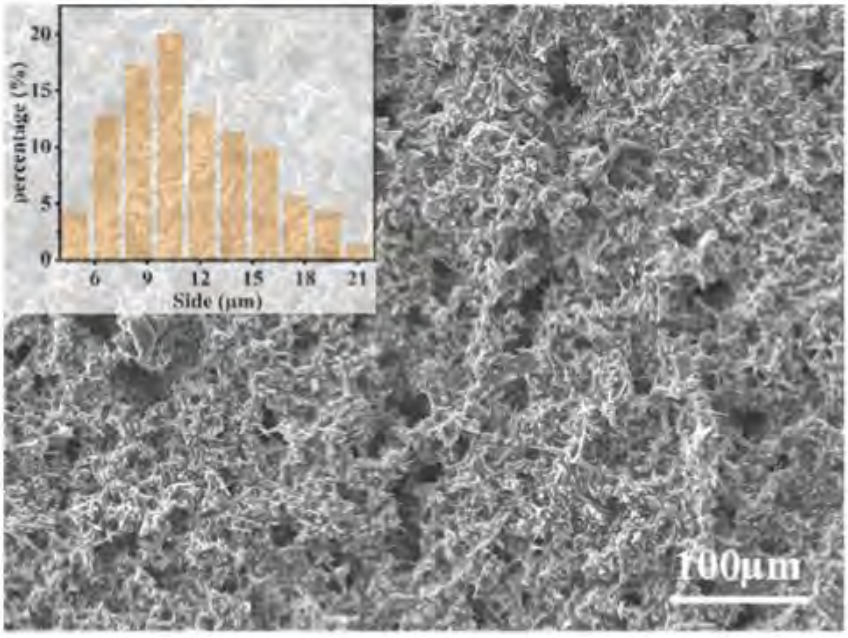

Figure S1. The surface SEM image of PTP film.

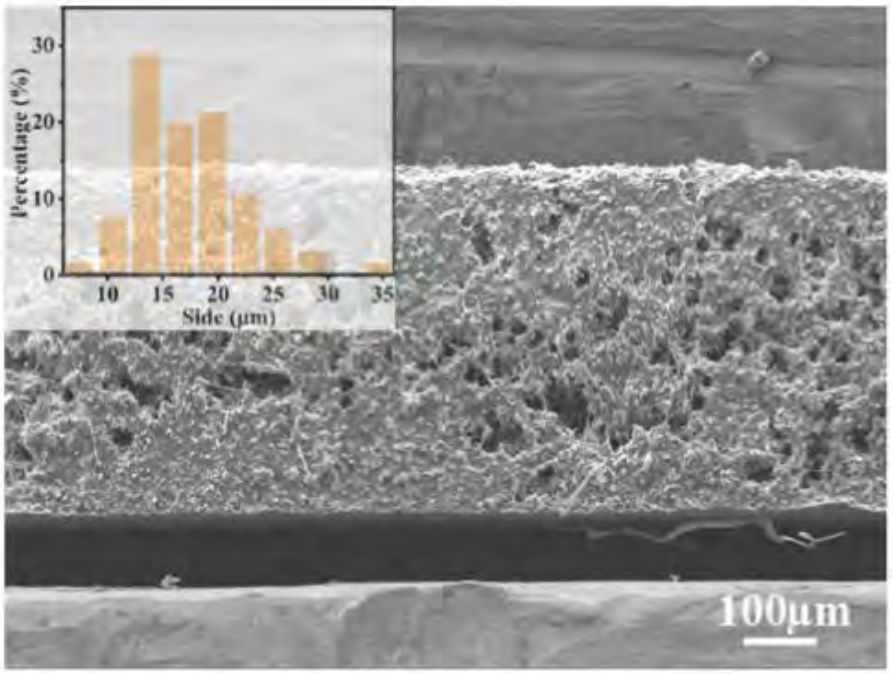

Figure S2. The cross-section SEM image of PTP film.

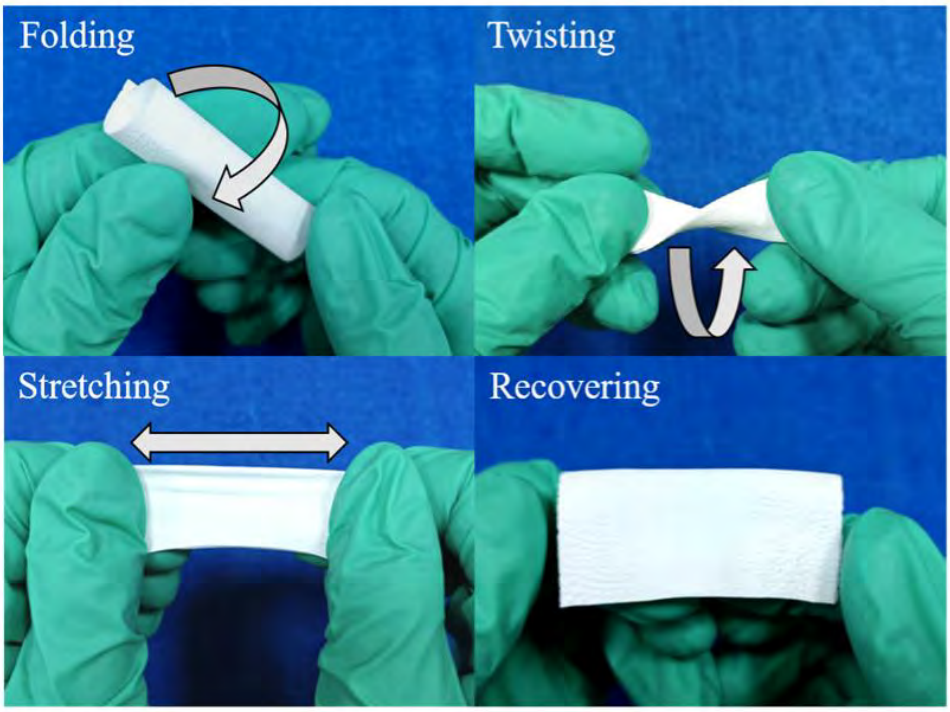

Figure S3. Flexibility test of PTP film.

From Figure S4, PDMS exhibits the largest elongation at break (41.8%), but a tensile strength of only 2 MPa. With increasing particle content, the elongation at break of the PTP films decreases, while the tensile strength increases. At a particle content of 60 wt%, the tensile strength reaches 8 MPa, four times higher than that of PDMS.

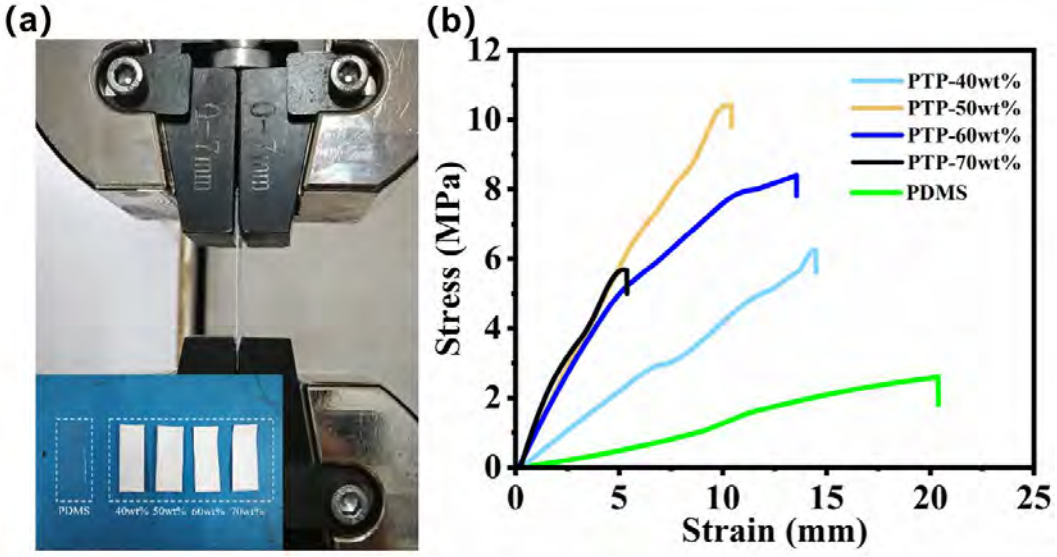

Figure S4. (a) Tensile strength test. (b) Stress-Strain image for different T-ZnOw mass fractions.

From Figure S5, the optical properties of PTP films have ideal impact resistance. Gravel impact testing is performed by repeatedly dropping 30 g of gravel from a height of 30 cm. After 30 impacts, the reflectance decreases from 0.9 to 0.89 (a reduction of 1%), while the emissivity decreases from 0.996 to 0.989 (a reduction of 0.7%).

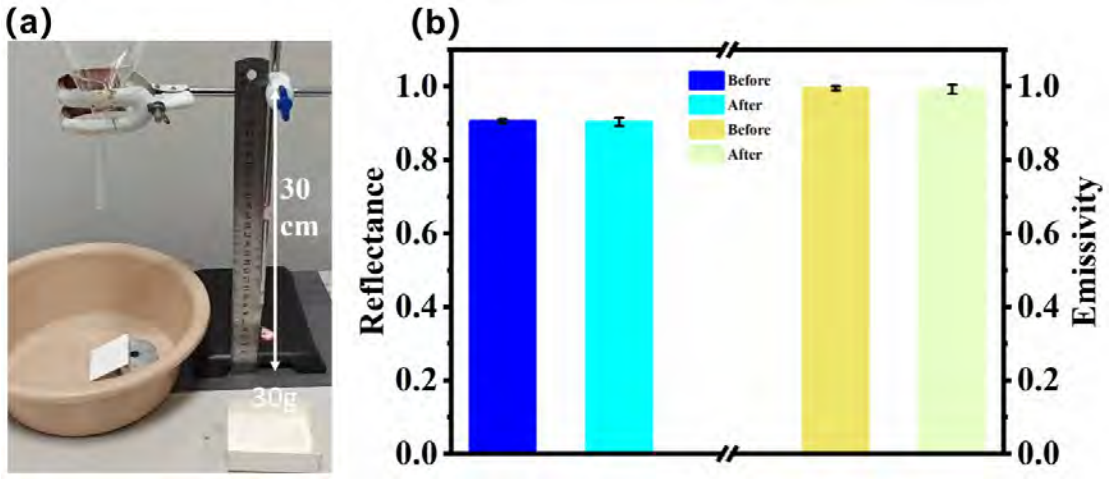

Figure S5. (a) Gravel impact resistance test. (b) Changes in reflectance and emissivity of PTP film before and after gravel impact.

From Figure S6, the optical properties of PTP films have ideal tensile resistance. After 100 tensile cycles, the reflectance decreases from 0.909 to 0.902 (a reduction of 0.7%), and the emissivity decreases from 0.993 to 0.988 (a reduction of 0.5%).

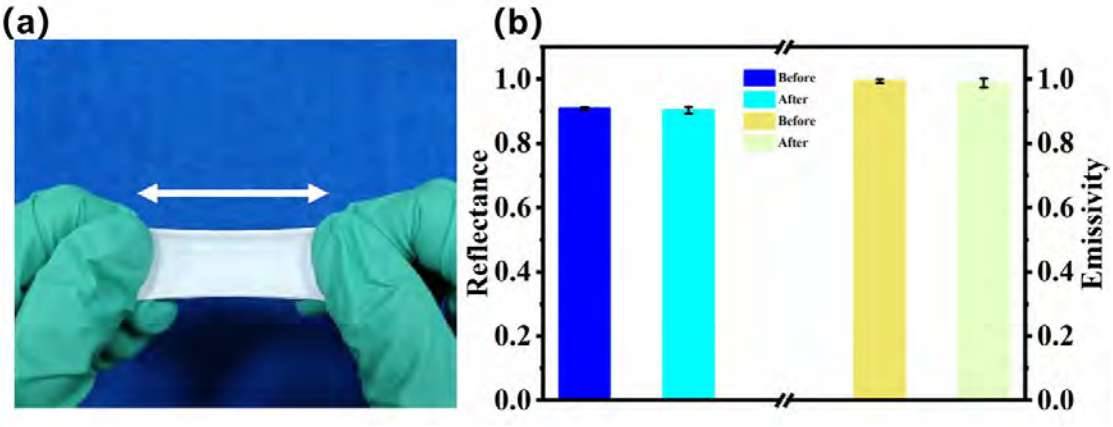

Figure S6. (a) Tensile cycle test. (b) Changes in reflectance and emissivity of the PTP film before and after tensile testing.

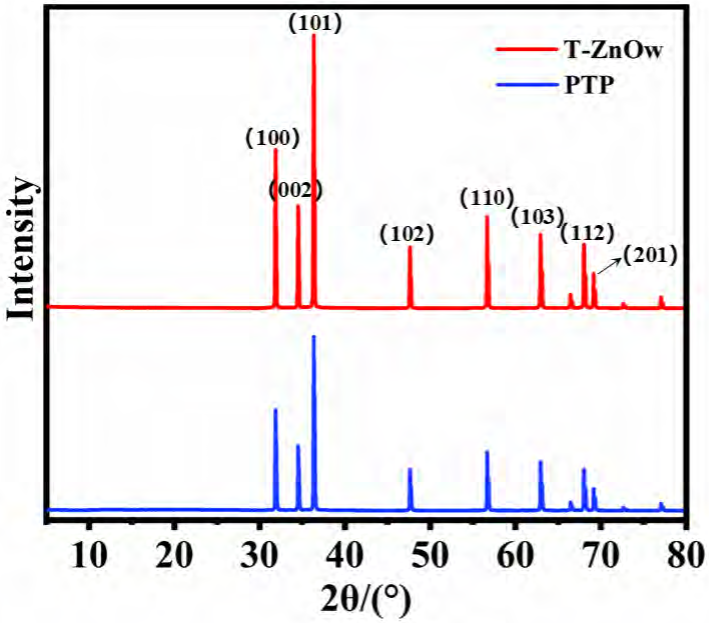

Figure S7. XRD patterns of PTP film and T-ZnOw particles.

.

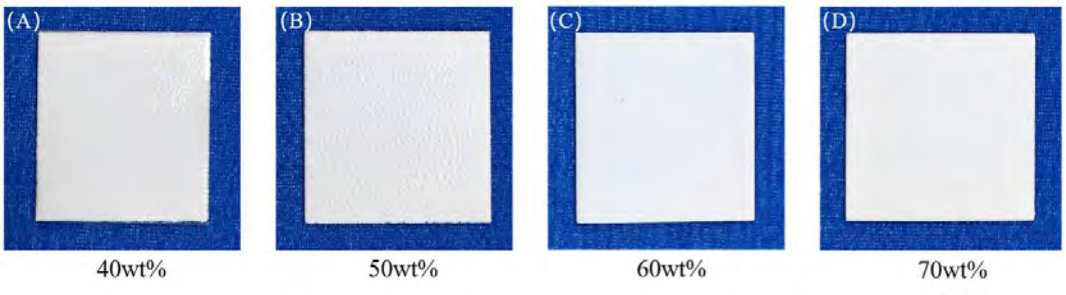

Figure S8. Optical pictures of PTP films with different particle mass fractions.

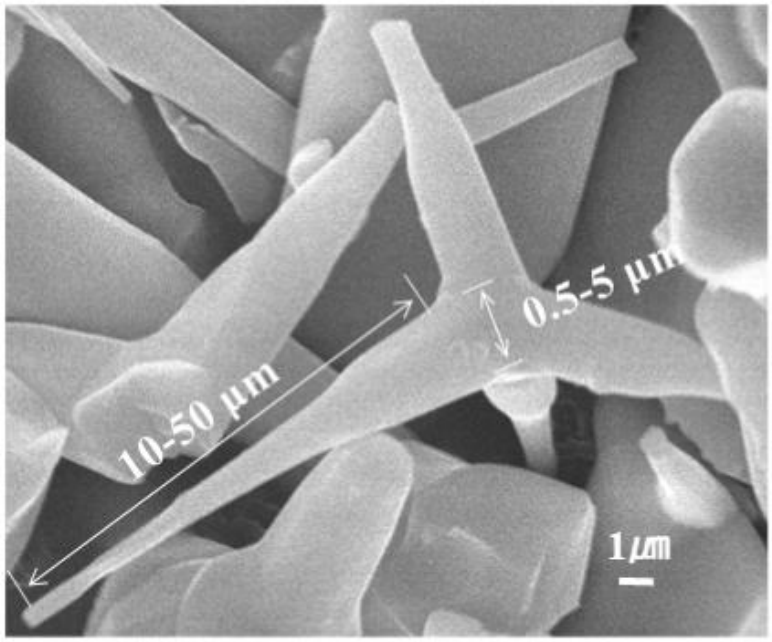

Figure S9. SEM image of T-ZnOw particles.

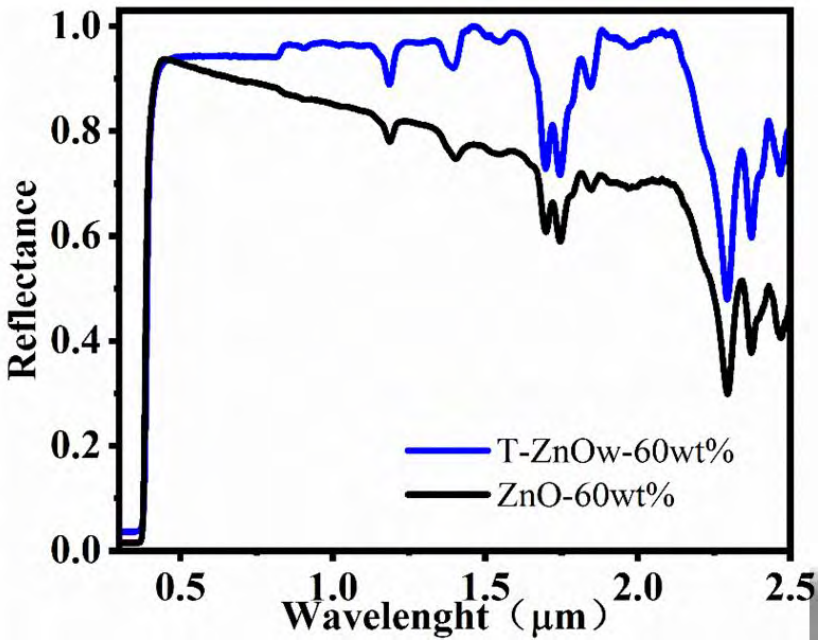

Figure S10. Comparison of reflectance of needle particles and ordinary particles composite films.

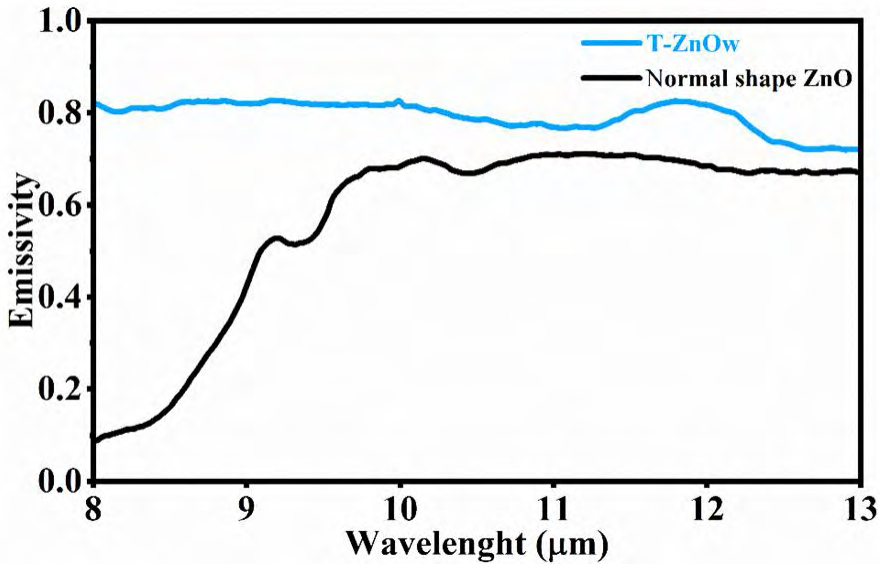

Figure S11. Comparison of emissivity of needle particles and normal shape particles.

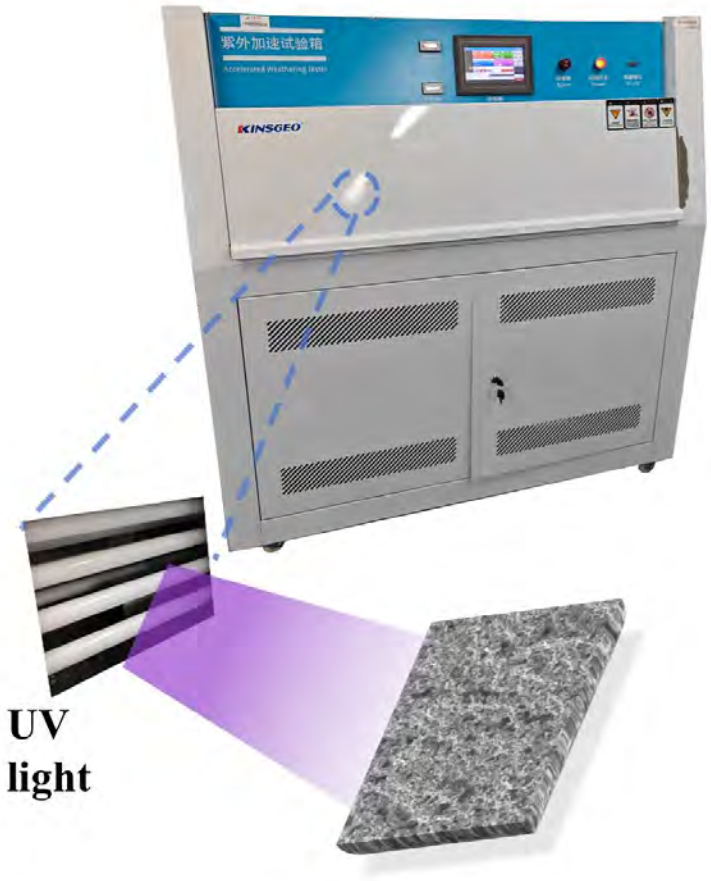

Figure S12. Schematic of UV aging assessment.

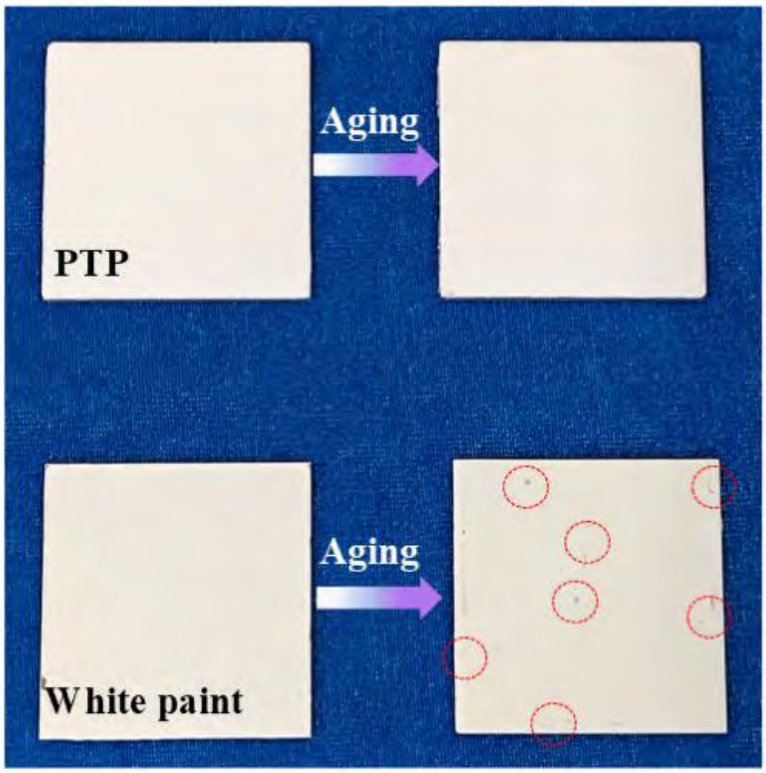

Figure S13. Optical photographs of PTP and white paint films before and after anti-aging.

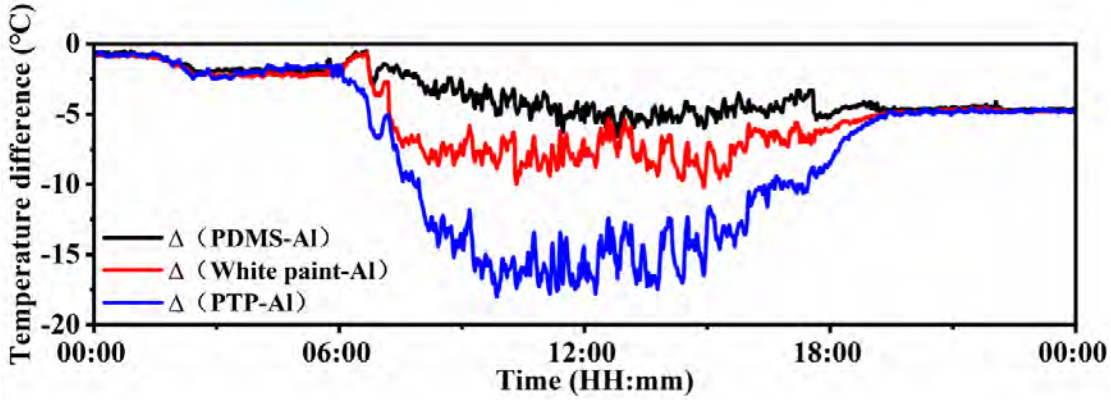

Figure S14. Temperature difference curves of the sealing PE film in the cooling test (June 12, 2024).

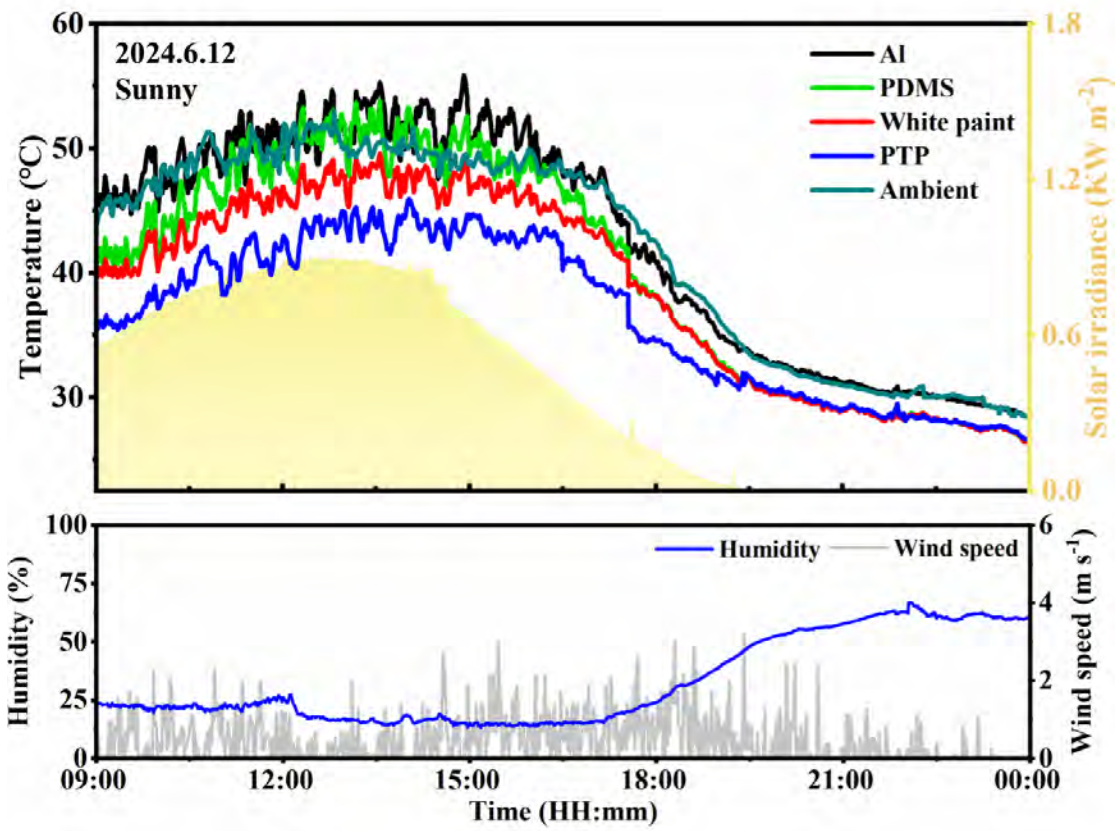

Figure S15. Unsealed PE film temperature curves, wind speed, and humidity (June 12, 2024).

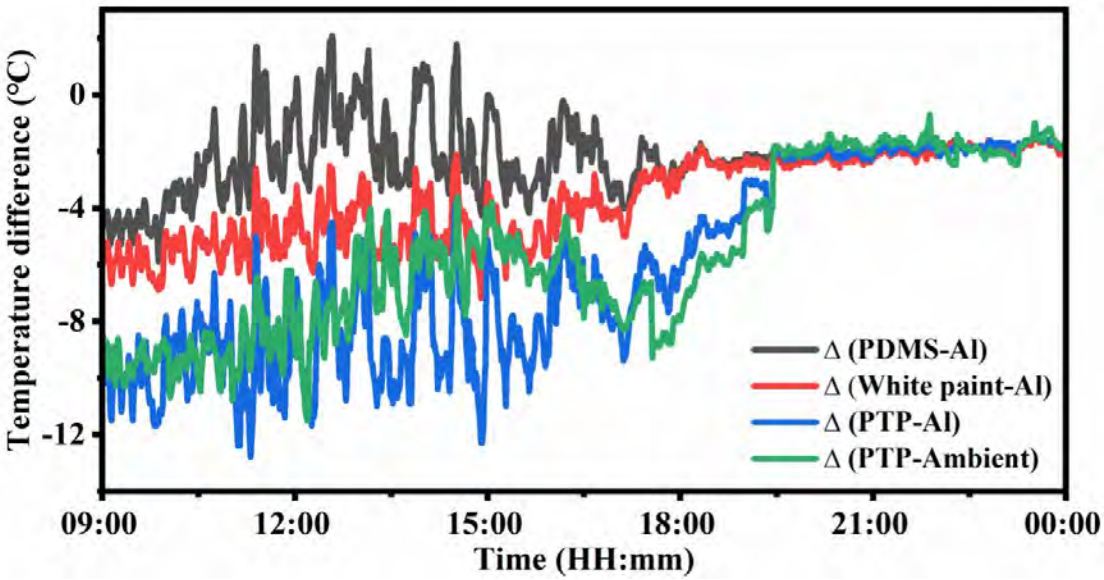

Figure S16. Temperature difference curves for the unsealed PE film temperature test (June 12, 2024).

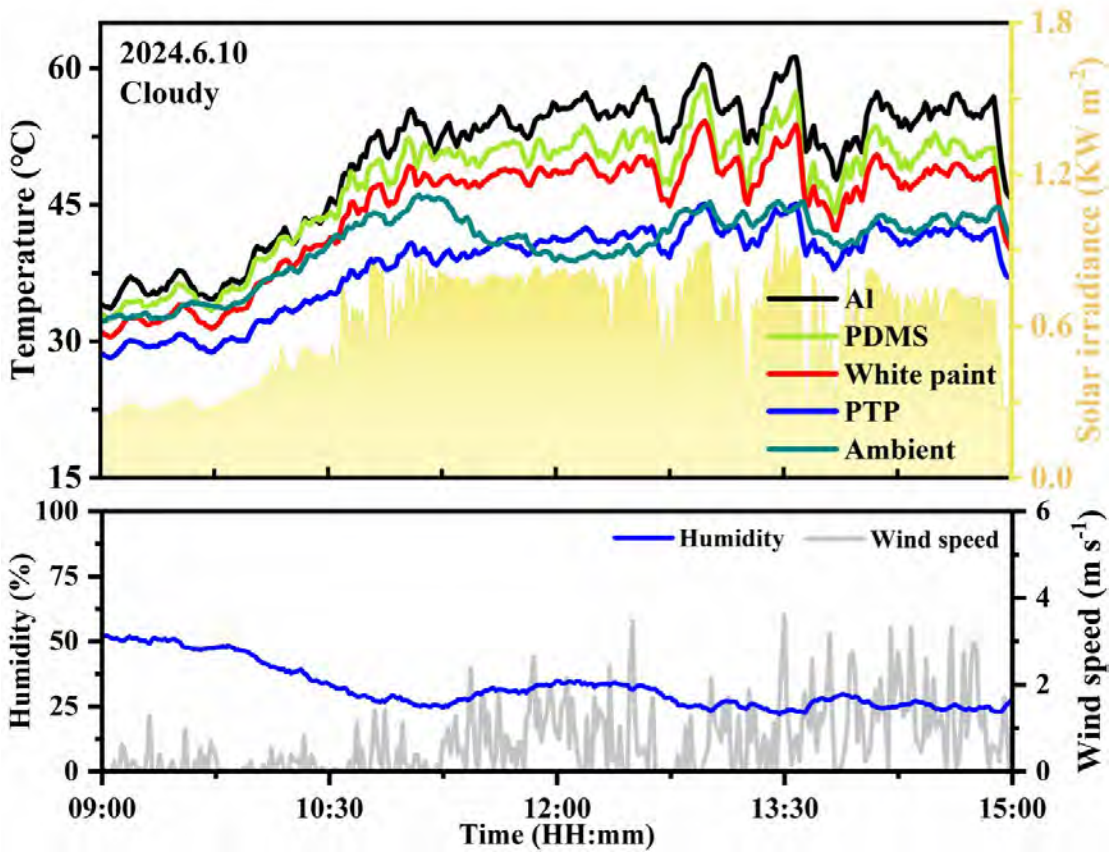

Figure S17. Temperature curves of the sealed PE film: cooling, wind speed, and humidity in cloudy weather (June 10, 2024).

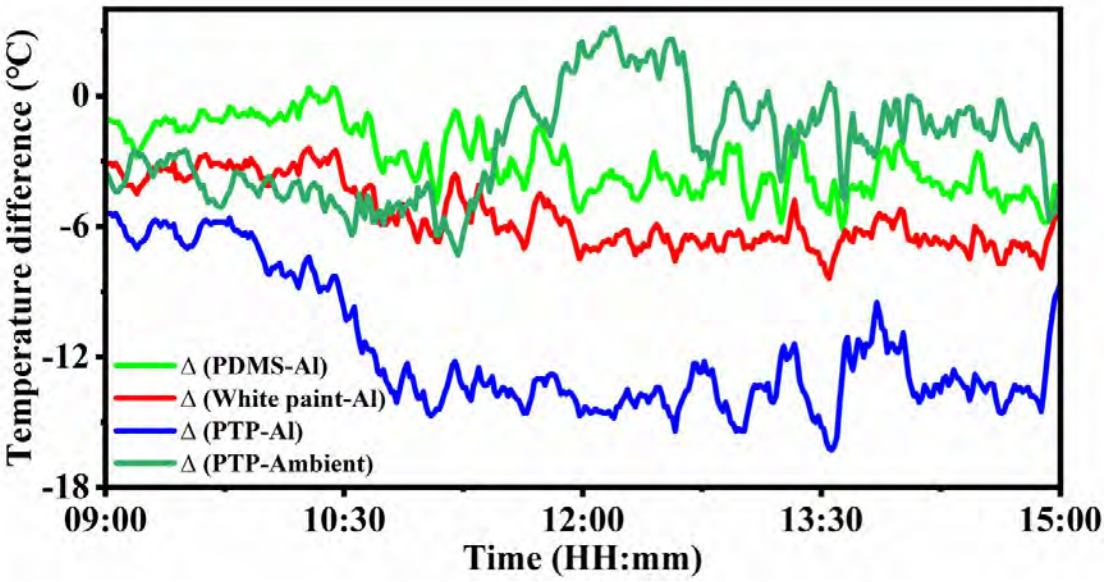

Figure S18. Temperature difference curves of the sealing PE film in the cooling test in cloudy weather (June 10, 2024).

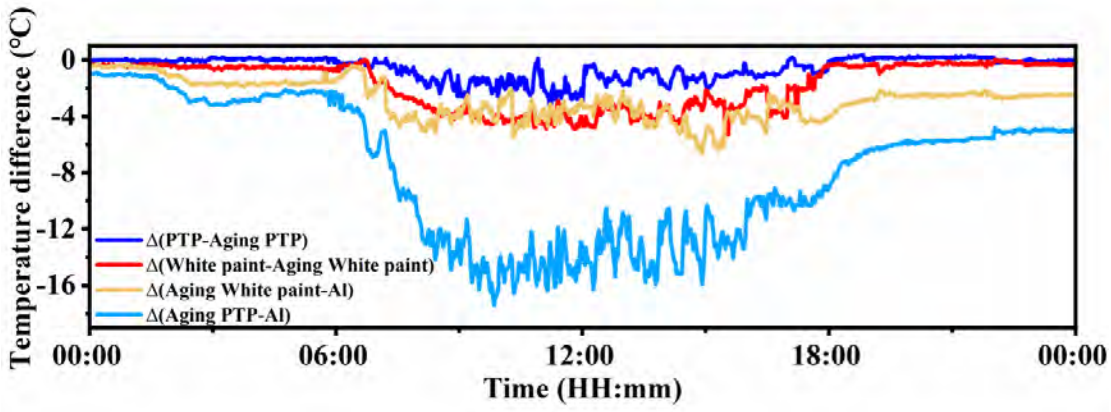

Figure S19. Temperature difference curves for the anti-aging cooling test (June 12, 2024).

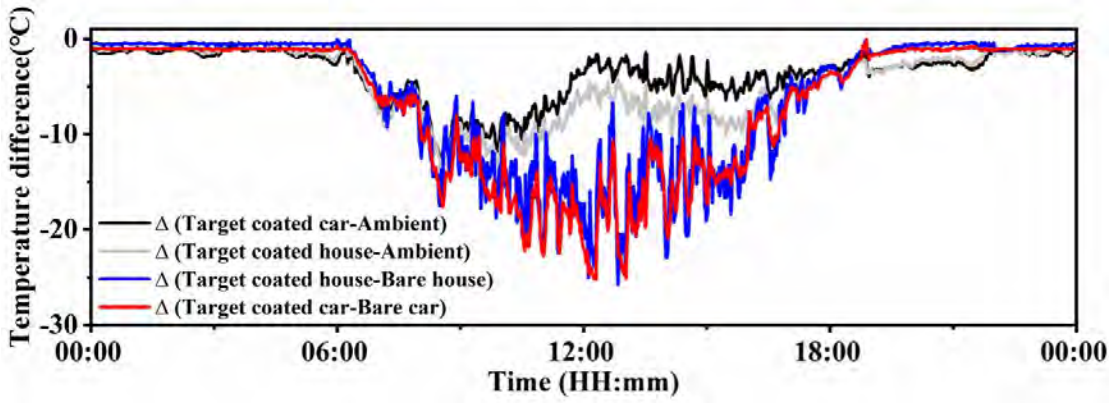

Figure S20. Temperature difference curves for the simulated cooling test (June 14, 2024).

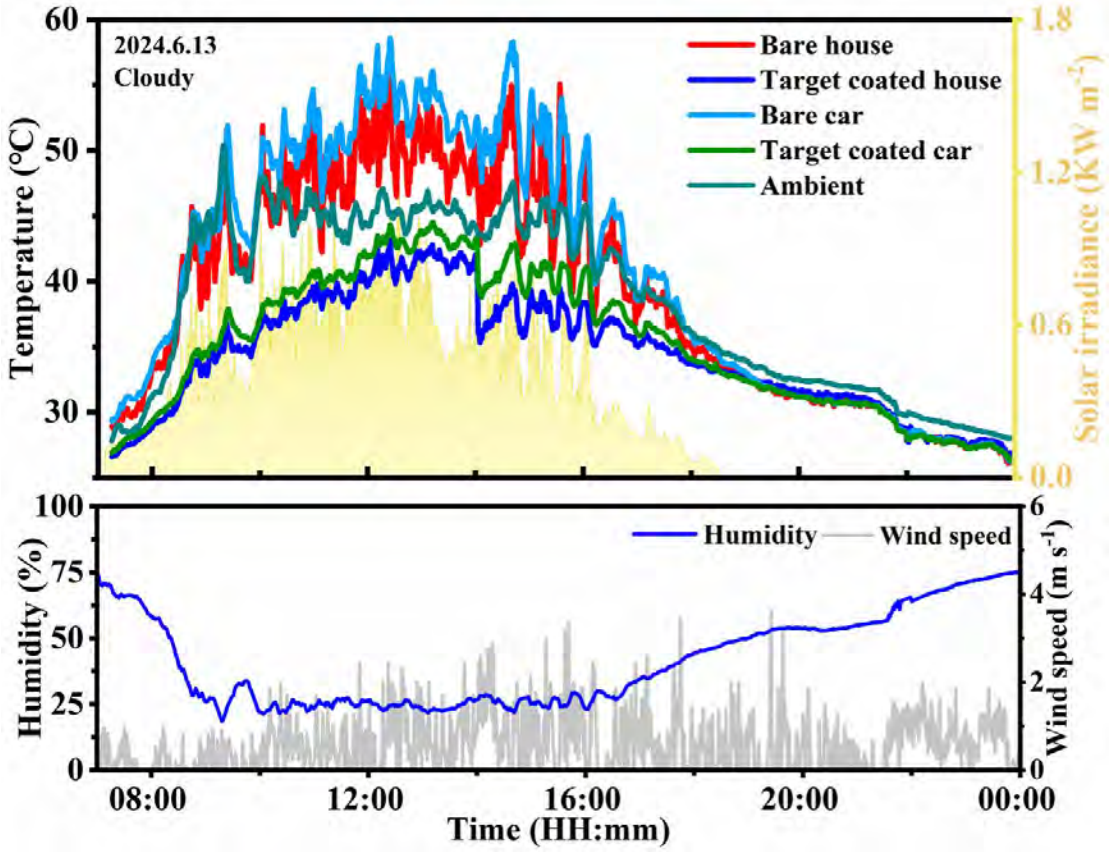

Figure S21. Temperature curves for the simulated cooling test, wind speed, and humidity on a cloudy day (June 13, 2024).

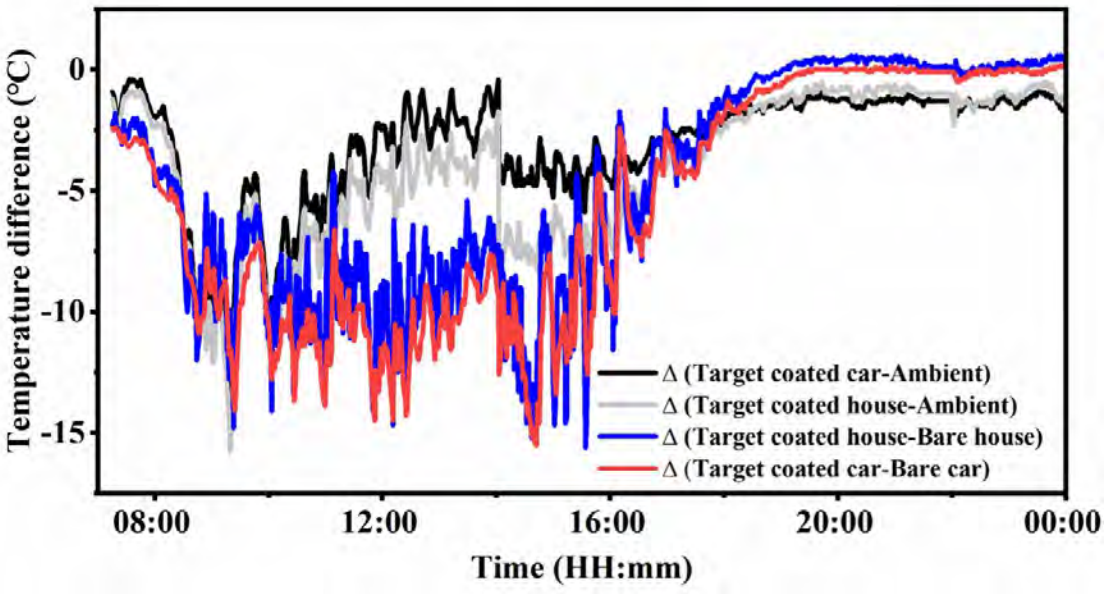

Figure S22. Temperature difference curves for the simulated cooling test (June 13, 2024).

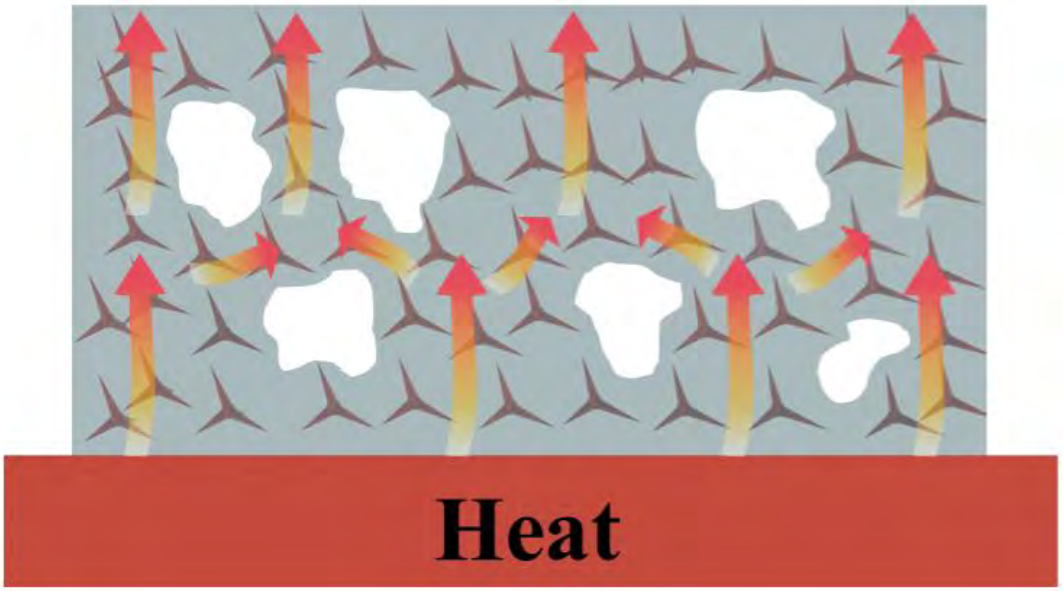

Figure S23. Schematic showing the thermal conductivity of the PTP film.

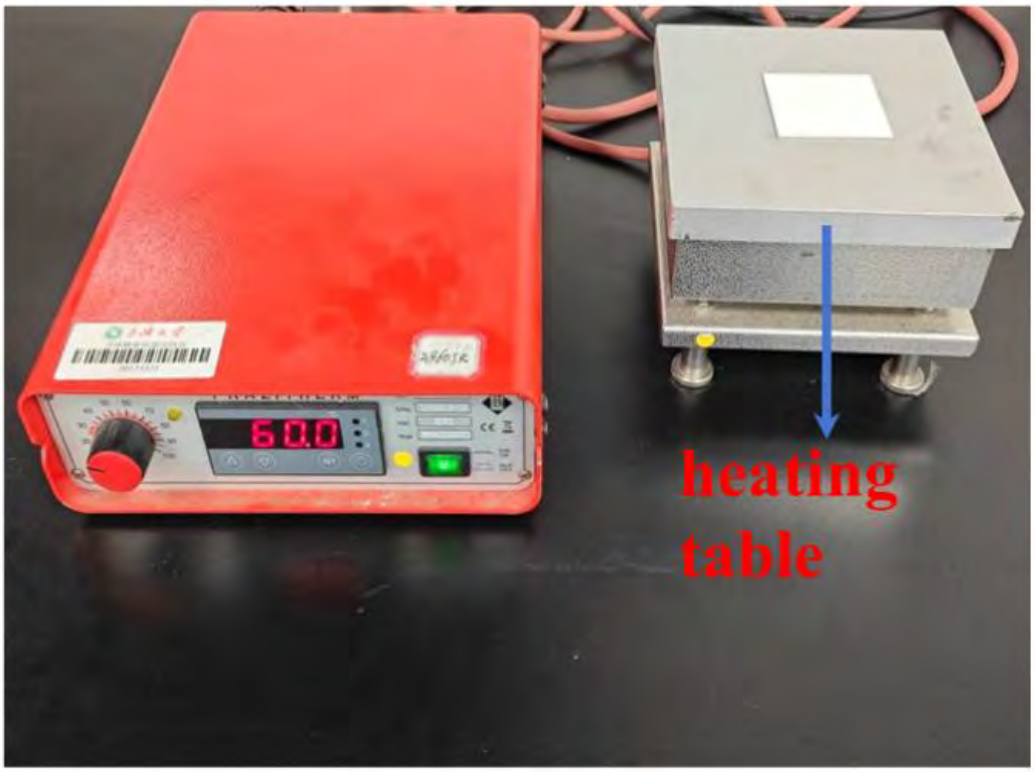

Figure S24. Laboratory heating table.

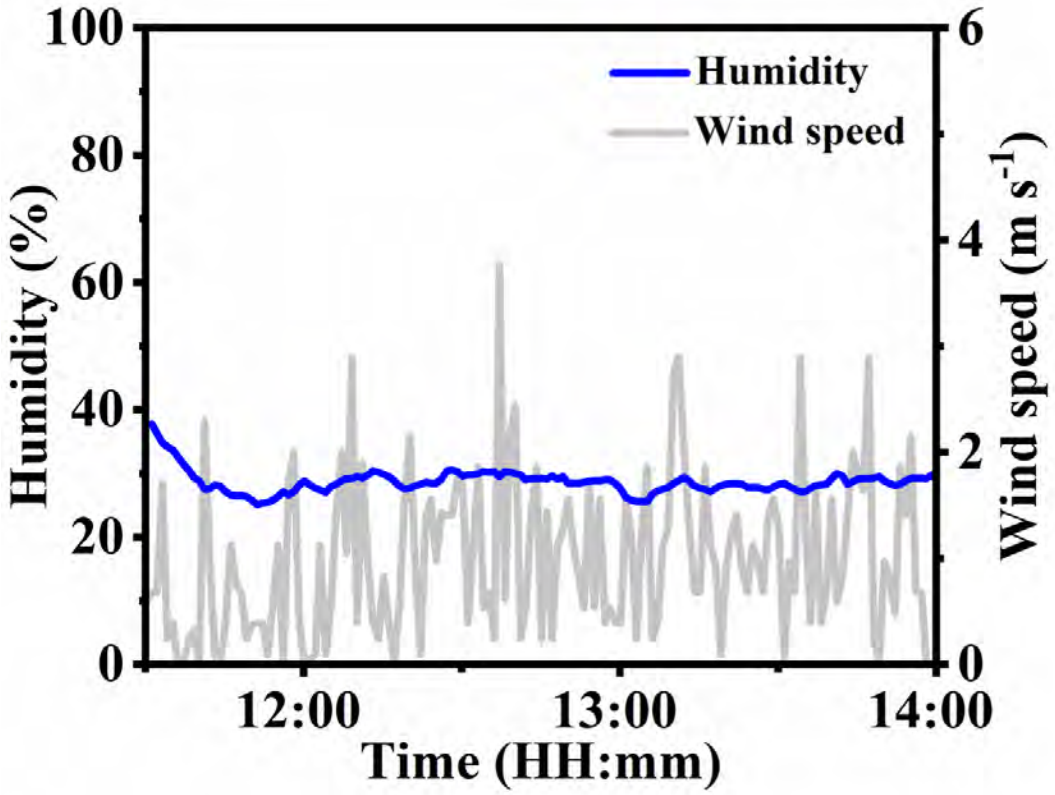

Figure S25. Wind speed and humidity at different times of the day during the cooling test with a heat source (June 11, 2024).

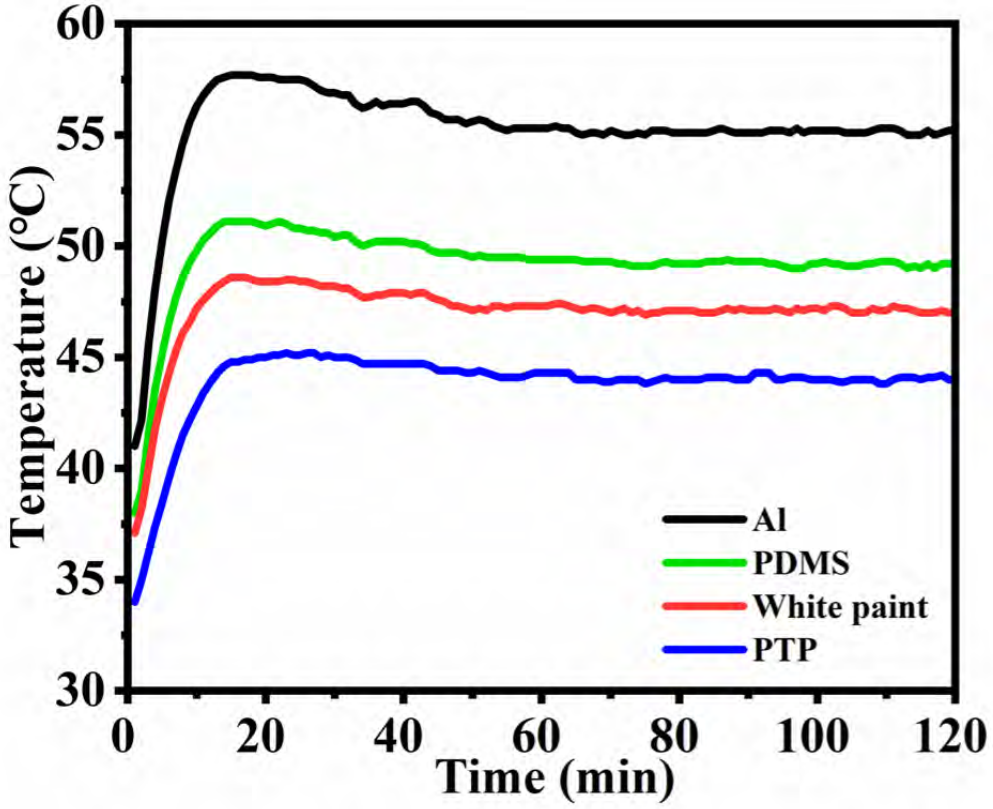

Figure S26. Indoor temperature test curves with a heat source.

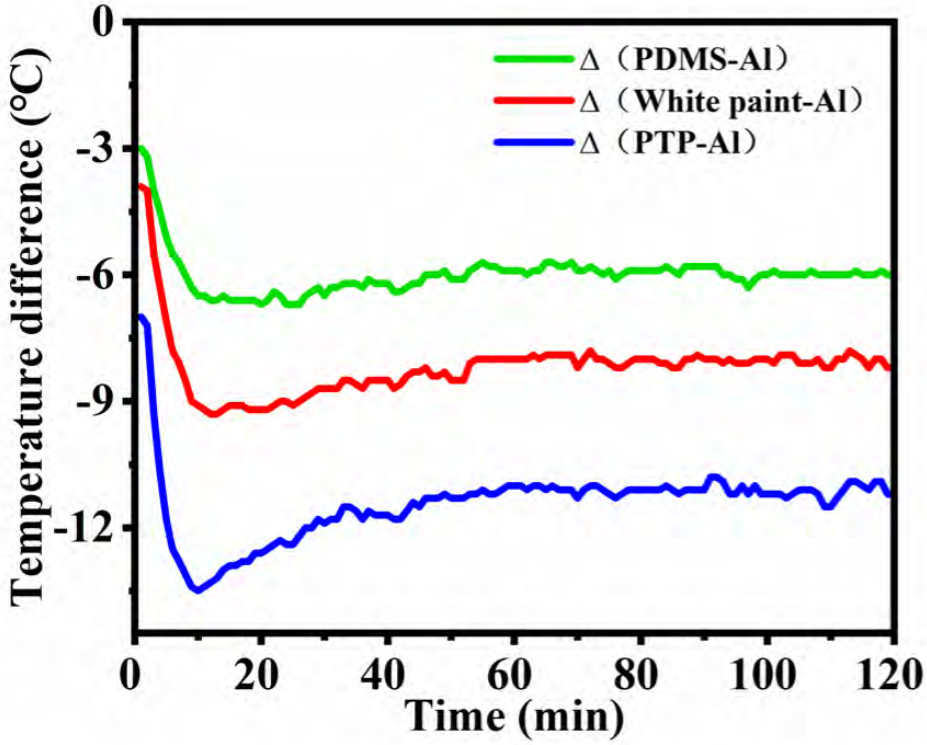

Figure S27. Temperature difference curves for the indoor cooling test with a heat source.

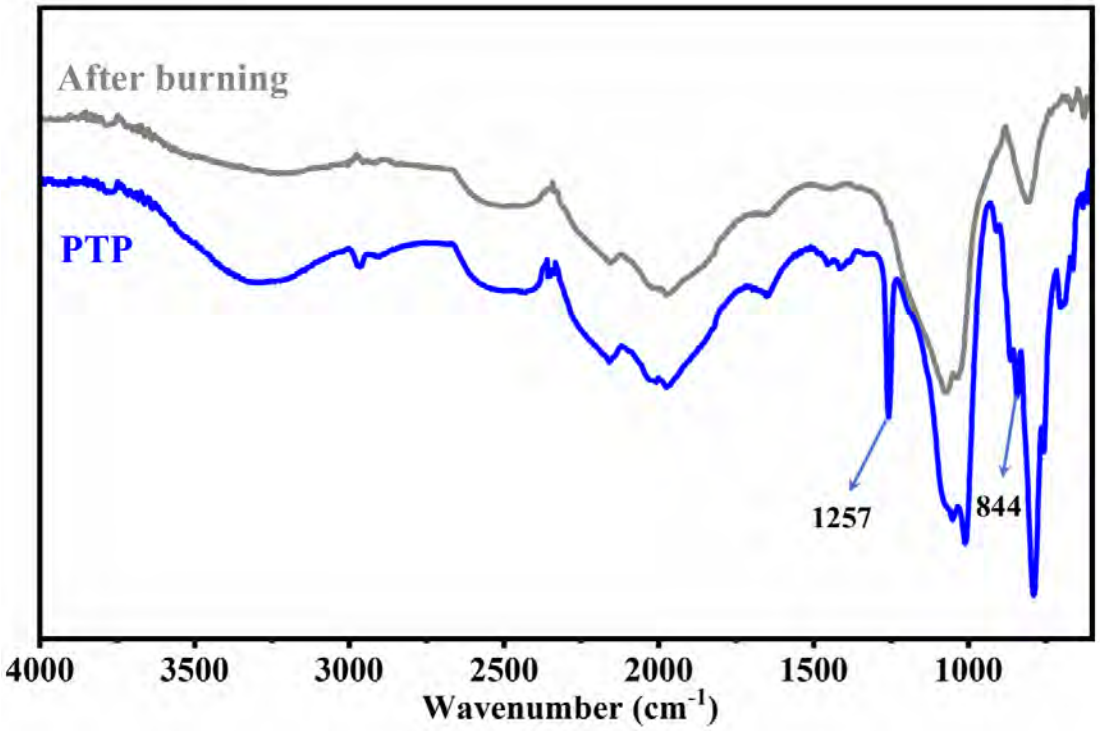

Figure S28. FTIR spectra of the samples before and after burning.

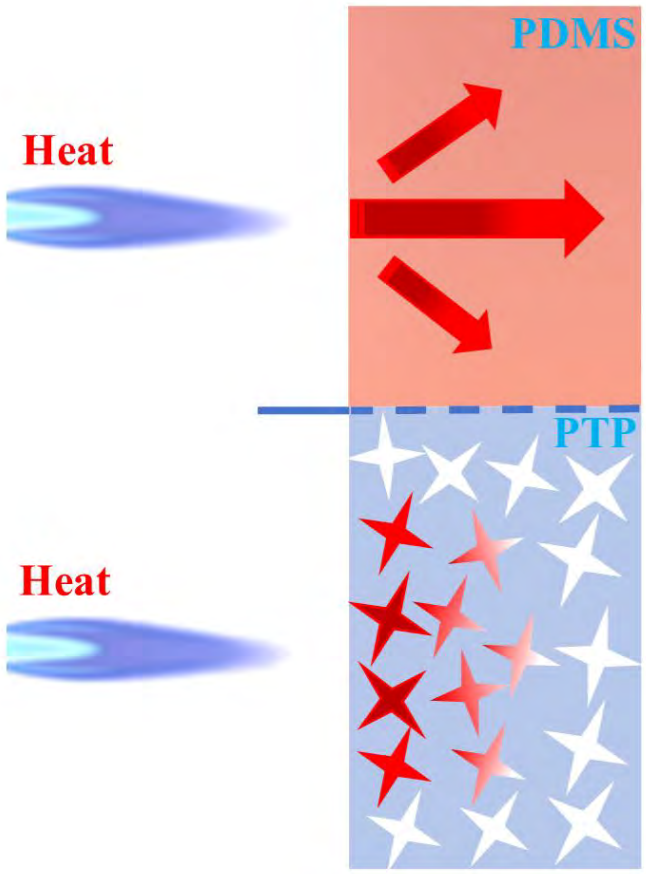

Figure S29. Schematic of the flame retarding principle.

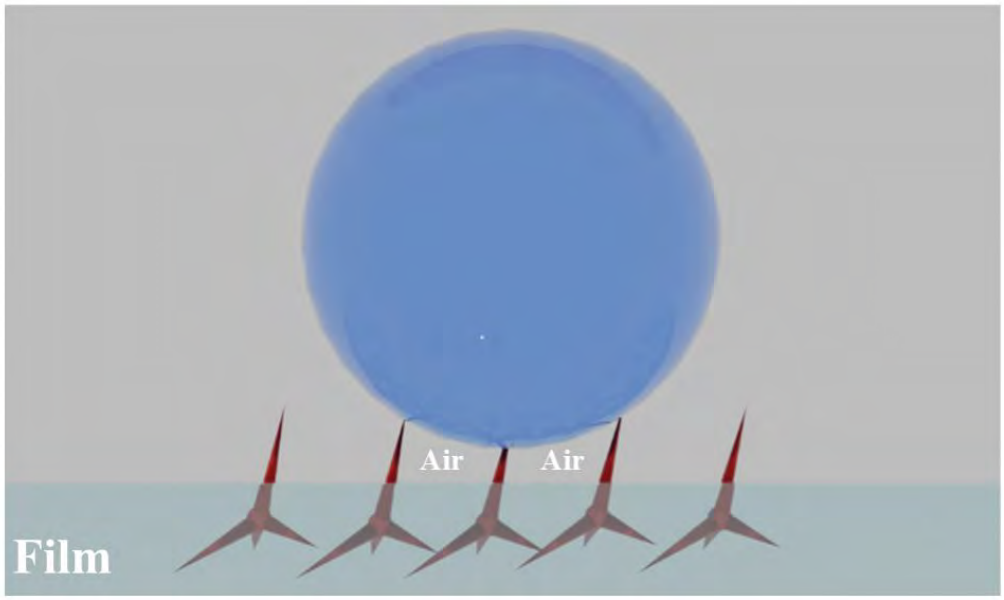

Figure S30. Schematic of hydrophobicity.

Table S1. Sealed PE film temperature differences (June 12, 2024).

	Δ = (PDMS-Al) /°C	**Δ = (White paint-Al) /°C**	**Δ = (PTP-Al) /°C**	**Δ = (PTP-Ambient) /°C**
Average temperature difference (Full time)	-3.5	-5.1	-8.0	-5.2
Average temperature difference (11:00-14:00)	-5.0	-7.5	-15.5	-7.0
Average temperature difference (20:00-23:59)	-4.6	-4.8	-4.8	-2.7
Maximum temperature difference	-5.8	-9.4	-17.7	-14.9

Table S2. Unsealed PE film temperature differences (June 12, 2024).

	Δ = (PDMS-Al) /°C	**Δ = (White paint-Al) /°C**	**Δ = (PTP-Al) /°C**	**Δ = (PTP-Ambient) /°C**
Average temperature difference (Full time)	-2.2	-3.7	-6.1	-5.6
Average temperature difference (11:00-14:00)	-1.3	-4.7	-8.9	-7.6
Average temperature difference (20:00-23:59)	-2.0	-2.0	-1.9	-1.8
Maximum temperature difference	-5.3	-7.2	-11.5	-10.5

Table S3. Sealed PE film temperature differences in cloudy weather (June 10, 2024).

	Δ = (PDMS-Al) /°C	**Δ = (White paint-Al) /°C**	**Δ = (PTP-Al) /°C**	**Δ = (PTP-Ambient) /°C**
Average temperature difference (Full time)	-3.6	-6.3	-13.5	-1.1
Average temperature difference (11:00-14:00)	-2.8	-5.3	-11.0	-2.2
Maximum temperature difference	-6.1	-8.4	-16.3	-7.3

Table S4. Anti-aging sealing PE film temperature differences (June 12, 2024).

	Δ = (PTP-Aging PTP) /℃	**Δ = (White paint-Aging White paint) /℃**	**Δ = (Aging PTP-Al) /℃**	**Δ = (Aging White paint-Al) /℃**
Average temperature difference (Full time)	-0.57	-1.8	-7.9	-2.8
Average temperature difference (11:00-14:00)	-1.5	-4.0	-13.8	-3.6
Average temperature difference (20:00-23:59)	-0.1	-0.3	-5.4	-2.5
Maximum temperature difference	-2.7	-4.9	-17.4	-6.4

Table S5. Temperature differences for simulated applications (June 14, 2024).

	Δ = (Target coated house-Bare house) /°C	**Δ = (Target coated car-Bare car) /°C**	**Δ = (Target coated house-Ambient) /°C**	**Δ = (Target coated car-Ambient) /°C**
Average temperature difference (Full time)	-6.2	-6.9	-4.6	-3.7
Average temperature difference (11:00-14:00)	-16.3	-18.2	-7.1	-4.2
Average temperature difference (20:00-23:59)	-0.7	-1.1	-1.7	-2.0
Maximum temperature difference	-25.8	-25.1	-15.1	-13.5

Table S6. Temperature differences for simulated applications in cloudy weather (June 13, 2024).

	Δ = (Target coated house- Bare house) /℃	**Δ = (Target coated car- Bare car) /℃**	**Δ = (Target coated house- Ambient) /℃**	**Δ = (Target coated car- Ambient) /℃**
Average temperature difference (Full time)	-4.8	-5.6	-4.0	-3.2
Average temperature difference (11:00-14:00)	-9.0	-10.5	-4.4	-2.8
Average temperature difference (20:00-23:59)	-0.3	-0.1	-1.0	-1.3
Maximum temperature difference	-15.6	-15.1	-15.8	-14.1

Table S7. Temperature differences in the presence of a heat source outdoors (June 11, 2024).

	Δ = (PDMS-Al) /℃	**Δ = (White paint-Al) /℃**	**Δ = (PTP-Al) /℃**
Average temperature difference (11:30-14:00)	-6.2	-10.3	-13.3
Max. temperature difference	-8.6	-13.4	-17.2

Table S8. Temperature difference with a heat source indoors (June 11, 2024).

	Δ = (PDMS-Al) /℃	**Δ = (White paint-Al) /℃**	**Δ = (PTP-Al) /℃**
Average temperature difference(120 min)	-4.5	-6.1	-9.1
Maximum temperature difference	-6.6	-9.2	-13.5